Carbohydrate Polymers 394 (2026) 126052



Contents lists available at ScienceDirect

Carbohydrate Polymers

journal homepage: www.elsevier.com/locate/carbpol



Distinct interfacial association of cellulose nanofibrils for enhanced mechanical strength and multiple functions of composite films via enzymatic tailoring of *Miscanthus* biomass

Ling Luo [a], Qian Zhang [a], Ji Shi [a], Guilan Zhao [a], Siqin Tan [a], Jiale Liu [a], Jingyuan Liu [a], Peng Liu [a], Hao Peng [a], Boyang He [b], Jing Wang [c], Hanluo Li [a], Yanting Wang [a], Hua Yu [a,*], Liangcai Peng [a,b,*]

[a] *Key Laboratory of Fermentation Engineering (Ministry of Education), Hubei Key Laboratory of Industrial Microbiology, Biomass & Bioenergy Research Center, School of Life & Health Sciences, Hubei University of Technology, Wuhan, 430068, China*
[b] *College of Plant Science & Technology, Huazhong Agricultural University, Wuhan, 430070, China*
[c] *Department of Ultrasound Medicine, Union Hospital, Tongji Medical College, Huazhong University of Science & Technology, Wuhan, Hubei, 430022, China*

ARTICLE INFO

Keywords:
Miscanthus accession
Cellulose nanofibers
Composite films
Enzymatic tailoring
Antioxidant activity
Food preservation

ABSTRACT

Although cellulose nanofibers (CNFs) are increasingly applied for a broad application, a knowledge gap remains about how CNFs are fundamentally associated with other nanomaterials for advanced films assembly with multiple functions and exceptionally high performances. By selecting desired *Miscanthus* lignocellulose, this study explores an enzymatic tailoring strategy to fabricate the eCNFs that consist of more and diverse defects on the fibril surfaces for interfacial association with diameter-varied lignin nanoparticles (LNPs). By incorporation with appropriate polyvinyl alcohol (PVA) and ε-polylysine (ε-PL), the selected PVA/5%eCNFs/ε-PL/15%LNPs film is constructed with enhanced mechanical performances such as the mostly raised rate (255.30%) of elongation at break and the second higher tensile strength (22.54 MPa) as a comparison with the previously-reported cellulose/lignin films, thereby enabling a mechanical stability after exposures of extreme temperatures (100 °C and − 80 °C). This film is also examined with significant improvements of UV-blocking ability, antioxidant activity and water/oxygen barrier property, leading to improved fresh-fruit preservation with reduced decay and deterioration during long term storage. Therefore, this study demonstrates a novel nanotechnology for desirable CNFs fabrication and it also provides insights into precise film design for specific function and implement.

1. Introduction

Through photosynthesis, plants produce abundant renewable lignocellulosic biomass that can be converted into valuable biomaterials (Wang et al., 2024; Zhang, Gao, Wang, et al., 2023). As two major polymers in lignocellulosic biomass, cellulose and lignin have been employed to generate functional nanomaterials for applications in multiple fields (Moreno & Sipponen, 2024; Österberg et al., 2023). Particularly, cellulose nanofibers (CNFs) are used as reinforced nanomaterials, whereas lignin nanoparticles (LNPs) are incorporated into composite materials for antioxidant activity and UV protection (He et al., 2023; Priyadarshi et al., 2024; Zhou et al., 2023). Despite CNFs and LNPs are integrated to generate the composite materials with high performance, much is yet unknown about how CNFs are associated with LNPs to enhance the mechanical strength and multiple functions in the composite materials, which thus hinders to explore advanced nanotechnology for desirable composite material construction (Moreno & Sipponen, 2024; Österberg et al., 2023; Zhou et al., 2023).

The growing environmental concerns associated with the extensive use of petroleum-based plastics have urged the development of sustainable, biodegradable, and high-performance alternatives (Turan et al., 2024; Upadhyay et al., 2024). Particularly, bio-based films are increasingly developed for flexible food packaging to reduce dependence on fossil-derived materials and to integrate multiple functions (Baishya et al., 2025; Zhang, Gao, Wang, et al., 2023). However, specifically targeting free-standing PVA-based flexible films for fresh-produce packaging still requires simultaneous improvements of mechanical and barrier properties, thermal stability, ultraviolet (UV)

* Corresponding authors.
E-mail addresses: yuhua@hbut.edu.cn (H. Yu), lpeng@mail.hzau.edu.cn (L. Peng).

https://doi.org/10.1016/j.carbpol.2026.126052
Received 25 August 2026; Received in revised form 4 November 2026; Accepted 18 November 2026
Available online 19 November 2026
0144-8617/© 2026 Elsevier Ltd. All rights are reserved, including those for text and data mining, AI training, and similar technologies.

shielding and antioxidant activity (Bhargava et al., 2020).

Polyvinyl alcohol (PVA) is a desirable film-forming polymer for the production of biodegradable materials because of its transparency, favorable mechanical properties, low toxicity and simple processing (Fan et al., 2025; Oun et al., 2022). Nevertheless, the PVA films often suffer from several drawbacks such as high hydrophilicity, limited moisture resistance and insufficient functional performance, which restricts their practical applications (Jailani et al., 2026; Kalita et al., 2025). To address these limitations, efforts have been made to incorporate nanocellulose (Lee et al., 2020), lignin-derived materials and other bio-based additives into PVA matrices (Haldar et al., 2026; Narasagoudr et al., 2020), and similar strategies have also been applied to construct functional food-packaging films (Zheng et al., 2024).

Among the various bio-based reinforcing materials, CNFs are particularly attractive due to their high aspect ratio, mechanical strength, biodegradability and abundant surface hydroxyl groups (Wang et al., 2016; Worku et al., 2024). These features enable CNFs to form dense and interconnected hydrogen-bonded networks within polymer matrices for improved mechanical strength and barrier performance (Hou et al., 2021). For examples, the nanocrystalline cellulose reinforces chitosan/guar gum films to reduce air permeability (Tang et al., 2018), whereas the combination of pristine CNFs and lignin-containing CNFs (L-CNFs) improves the mechanical, barrier, UV-shielding, and antioxidant properties of composite films (Trifol & Moriana, 2022). The L-CNFs with regulated residual lignin content are also incorporated with PVA and alkyl ketene dimer to enhance the mechanical strength and barrier performance of composite films (Deng et al., 2025). Meanwhile, LNPs have emerged as promising functional fillers, owing to their polyphenolic aromatic structures and UV-shielding and antioxidant properties (Priyadarshi et al., 2024). Compared with non-nanosized lignin, LNPs generally exhibit better dispersibility and larger specific surface areas, potentially facilitating interactions with CNFs and other polymers (Moreno & Sipponen, 2024; Österberg et al., 2023). The incorporation of a wood cellulose skeleton and LNPs into PVA films improves flexibility and UV shielding (Zhou et al., 2023), and the incorporation of LNPs into CNFs films enhances UV-shielding, antioxidant activity and raspberry preservation (Las-Casas et al., 2025). A laccase-catalyzed oxidative crosslinking is also used to improve interfacial integrity and oxygen barrier performance in L-CNFs/LNPs coatings (Babaeipour et al., 2025). Since intermolecular interactions also affect multicomponent films, the ε-polylysine (ε-PL), an amino-rich cationic biopolymer, is incorporated for its antimicrobial potential and compatibility with biopolymer matrices (Han et al., 2025; Yang et al., 2024). Thus, PVA, CNFs, ε-PL and LNPs are increasingly selected for film formation, reinforcement, potential antimicrobial activity, UV-shielding and antioxidant functions.

Miscanthus is a dedicated bioenergy crop because of its rapid growth, diverse lignocellulosic composition and well adaptation to various environments (Gao et al., 2026; Q. Li et al., 2019; Yu et al., 2026). The distinct lignocellulosic composition and cellulose degree of polymerization (DP) among *Miscanthus* accessions provide an opportunity to examine whether the structural characteristics of CNFs regulate their interfacial association with LNPs. We hypothesized that mixed-cellulase treatment could concurrently modify cellulose DP, surface morphology, and residual polysaccharide composition of CNFs, and these coupled changes might affect CNFs association with LNPs for composite film performance. To test this hypothesis, two *Miscanthus* accessions (Msa10 and Msa32) with distinct lignocellulosic compositions and cellulose DP values were selected. Ball milling, high-pressure homogenization and mixed-cellulase hydrolysis were then employed to generate the enzymatically-tailored CNFs (eCNFs) with altered DP, surface morphology and chemical composition (Fig. S1). Meanwhile, LNPs were prepared from commercial alkaline lignin and subsequently integrated with CNFs/eCNFs, PVA and ε-PL to construct composite films. Given previous studies have explored lignin retention, direct CNFs and LNPs incorporation, and laccase-mediated crosslinking, this study specifically explored a conceptual model about enzymatically-tailored eCNFs association with LNPs for advanced composite films (Fig. 1).

2. Materials and methods

2.1. Materials

Two *Miscanthus* (Msa10 and Msa32) accessions were harvested from the Experimental Station of Huazhong Agricultural University (Wuhan, China). The well-dried straw was milled into powder using a QE-300 grinder (Zhejiang Yili Industry and Trade Co., Ltd., China), passed through a 40-mesh sieve (425 μm), and stored until use. Alkali lignin and authentic standards of *p*-hydroxybenzaldehyde (H-type), vanillin (G-type), and syringaldehyde (S-type) were purchased from Aladdin Biochemical Technology Co., Ltd. (Shanghai, China). ε-Polylysine (ε-PL; MW < 5000 Da) and cupriethylenediamine solution (CED, 1.0 mol/L in H_2O) were obtained from Macklin Biochemical Technology Co., Ltd. (Shanghai, China). Polyvinyl alcohol (PVA, degree of polymerization 1750 ± 50, 98% hydrolysis) and glycerol (purity ≥99%) were supplied by Sinopharm Chemical Reagent Co., Ltd. (Shanghai, China). Cherry tomatoes were obtained from local market (Wuhan, China).

2.2. Preparation and detection of wall polymers

Plant cell wall fractionation was performed to extract major wall polymers as described (Li et al., 2026; Lu et al., 2026). Hexoses and pentoses of carbohydrates were detected using a UV–vis spectrophotometer (V—1100D, Shanghai MAPADA Instruments Co., China) (Gao et al., 2026; Yu et al., 2022; Yu et al., 2025). Total lignin content was assessed by two-step acid hydrolysis method (Yu et al., 2026). For crude cellulose preparation, about 0.3 g *Miscanthus* powder was immersed with 10.0 mL 8.0% (*w/v*) $NaClO_2$ containing 1.5% acetic acid (Zhang, Hu, Peng, et al., 2023). The well-mixed solution was shaken horizontally under 150 rpm shaking at 25 °C for 48 h along with the $NaClO_2$ solution replaced every 12 h. The residue was washed with distilled water until pH 7.0, and treated with 10.0 mL 4.0 mol/L KOH under 150 rpm shaking at 25 °C for 2 h. The solid residue was thoroughly washed with distilled water until pH 7.0, dried at 60 °C and stored as crude cellulose sample.

2.3. Preparation and characterization of CNFs and LNPs

2.3.1. Preparation of CNFs and LNPs

For preparation of enzymatically-tailored eCNFs, about 3.5 g crude cellulose (CFs) sample was dispersed in 35 mL distilled water, and milled in a planetary ball mill (BM40, Beijing Grinder Instrument Co., Ltd., China) at 300 rpm shaking for 5 h. The resulting suspension was processed using a high-pressure homogenizer (UH-20, Union-Biotech Co., Ltd., Shanghai, China) at 600 bar for 20 cycles to obtain the initial CNFs suspension (Peng et al., 2022). The CNFs suspension was incubated with commercial mixed-cellulases (HSB, Imperial Jade Biotechnology Co., Ltd., Ningxia, China; β-glucanase ≥3.0×10^4 U/g, cellulase ≥3.0×10^4 U/g, and xylanase ≥5.0×10^4 U/g) on the basis of enzyme-to-CNFs mass ratio of 1:40 (Yang et al., 2026). The enzymatic hydrolysis was carried out at 50 °C with horizontal shaking at 150 rpm for 1 h and 2 h, respectively. The reaction was terminated by immersing the sample in a boiling water bath (100 °C) for 5 min. The resulting suspension was centrifuged at 3000 *g* for 10 min, and the recovered solids were washed ten times with deionized water. The washed solids were redispersed in deionized water and designated as eCNFs for composite film preparation. The eCNFs yield was calculated as the dry mass of recovered eCNFs divided by the initial dry mass of CNFs and expressed as a percentage. The concentration of the eCNFs suspension was determined gravimetrically. Approximately 3 g of suspension (m_{wet}) was placed in a pre-weighed centrifuge tube (m_{tube}) and dried at 60 °C to a constant total mass (m_{dry}). The concentration (wt%) was calculated using the following eq. (1):

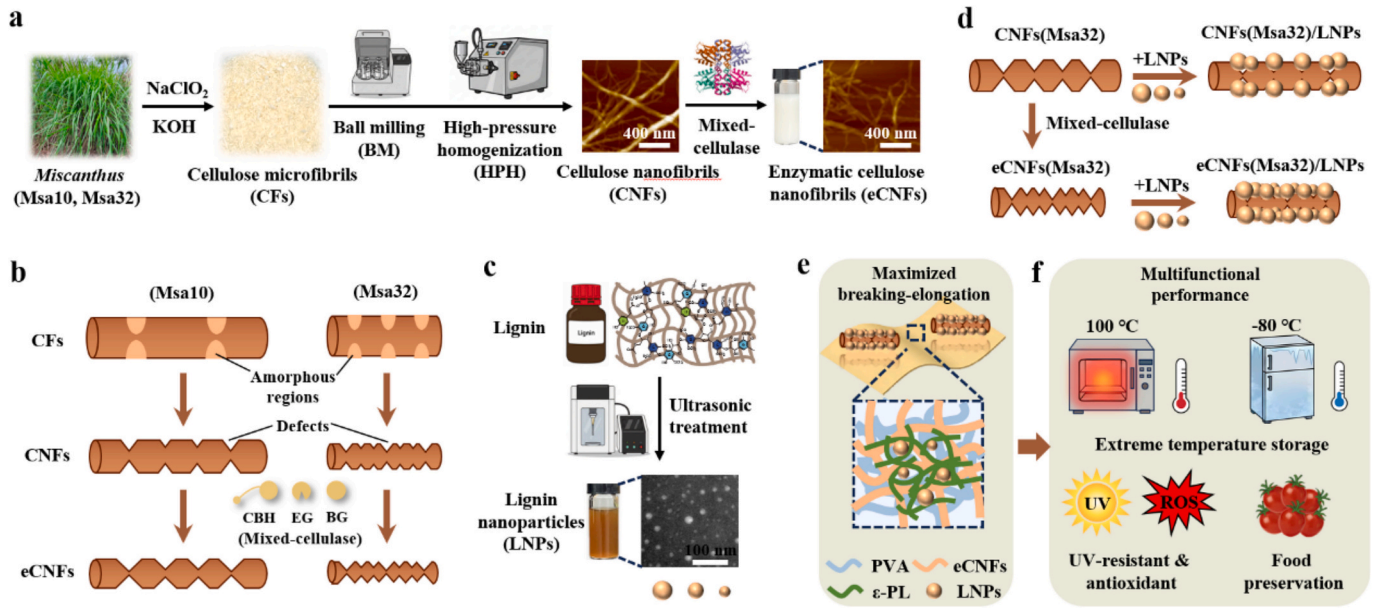


Fig. 1. Overview of composite films assembly and fabrication. (a) Preparations of CNFs and eCNFs from two *Miscanthus* accessions (Msa10, Msa32) straws. (b) Structure modes of CFs, CNFs and eCNFs formations. (c) Preparation of LNPs from alkali lignin. (d) Proposed schematic illustration of interfacial association between CNFs/eCNFs and LNPs. (e) Assembly model of the selected PVA/5%eCNFs/ε-PL/15%LNPs composite film. (f) Multifunctional performance of the selected film, including mechanical stability after 100 °C exposure and − 80 °C storage, UV shielding and radical-scavenging activity, and cherry tomato packaging performance.

$$C(wt\%) = \frac{m_{dry} - m_{tube}}{m_{wet}} \times 100 \quad (1)$$

The LNPs preparation was conducted as described (Wan et al., 2025). About 0.4 g alkali lignin was dispersed in 39.6 mL distilled water, and stirred under 300 rpm at 25 °C for 10 min. The resulting suspension was sonicated using an ultrasonic homogenizer (SCIENTZ-IID, Ningbo Scientz Biotechnology Co., Ltd., China) at 500 W for 3 h as LNPs dispersion.

2.3.2. Detection of degree of polymerization of CNFs

The degree of polymerization (DP) of CNFs was estimated by viscometry method, using a Ubbelohde viscometer (Taizhou Jiaojiang Huanguang Glass Instrument Co., Ltd., Taizhou, China) with a range of 0.7 mm - 0.8 mm (Gao et al., 2026). Approximately 0.05 g of dried sample was dissolved in 10.0 mL of 1.0 mol/L CED solution at 25 °C under shaking (150 rpm) for 12 h under dark. After centrifugation at 3000 *g* for 5 min, the solution was equilibrated at 25 ± 0.1 °C for 30 min. The relative viscosity (η_{rel}) was calculated as t/t_0, where t and t_0 were the efflux times of the cellulose solution and solvent blank, respectively. The intrinsic viscosity ([η]) was obtained from η_{rel} and the dissolved cellulose concentration using the viscosity tables in USP 25-NF 20 (United States Pharmacopeial Convention, 2002). The cellulose concentration (C, g/100 mL) was calculated using the following eq. (2):

$$C = \frac{W_1 - W_2}{V} \quad (2)$$

Where W_1 and W_2 are the initial dry sample mass and dried insoluble residue mass, respectively, and V was the CED volume (mL). The viscosity-based DP was obtained using the modified Grobe eq. (3):

$$DP = 190 \times [\eta] \quad (3)$$

The corresponding molecular weight (M) was estimated from cellulose DP according to the following eq. (4) (Sun et al., 2026; Yu et al., 2024):

$$M = DP \times 0.162 \quad (4)$$

Where 0.162 kDa represents the molecular weight of one glucose unit.

2.3.3. Morphological characterization of CNFs and LNPs

The micro-morphologies of CNFs and LNPs were respectively observed under a transmission electron microscope (TEM, HT-7800, Hitachi, Japan) at an accelerating voltage of 100 kV. Prior to observations, the CNFs and LNPs suspensions were diluted with deionized water to concentrations of 0.005 wt% and 0.01 wt%, respectively, followed by ultrasonic treatments for 30 min. A droplet of each dispersion was deposited onto a copper grid and negatively stained with 1.5 wt% phosphotungstic acid for 15 min under dark. The dimensions of the nanomaterials were subsequently detected using ImageJ software.

Characterization of CNFs defects was performed as described (Peng et al., 2022). The CNFs was diluted to 0.01% (*w/v*) with distilled water, and about 2 μL aliquot of the diluted suspension was deposited onto a freshly cleaved mica surface and dried at 25 °C. The morphological characteristics were observed by atomic force microscopy (AFM, Bruker Dimension Edge, Germany) at a scanning rate of 1 Hz. The apparent lateral fibril widths, surface defect widths, local height differences, and inter-defect distances were measured from AFM images using Gwyddion software. The apparent lateral fibril widths were determined from line profiles perpendicular to the fibril axes. Surface defects were defined as local depressions or irregularities in the AFM height profiles. The AFM-derived lateral widths were considered apparent values due to potential tip-convolution effects and were distinguished from the TEM-derived fibril diameters.

2.3.4. Characterization of LNPs and CNFs/LNPs suspensions

The monomer composition of alkali lignin was determined by nitrobenzene oxidation following the method described (Gao et al., 2026), followed by high-performance liquid chromatography (HPLC) analysis. The oxidation products were analyzed using a Shimadzu LC-20A HPLC system (Shimadzu, Japan) equipped with a UV detector at 280 nm and a Kromat Universal C18 column (4.6 × 250 mm, 5 μm). The mobile phase consisted of methanol, water, and acetic acid (16:63:1, *v/v/v*), with a flow rate of 1.1 mL/min and an injection volume of 20 μL. The relative proportions of H-, G-, and S-type monomers were expressed as percentages of their total content. Three independently weighed lignin samples were separately subjected to nitrobenzene oxidation and HPLC analysis.

CNFs and LNPs were mixed at mass ratios of 1:1, 1:2, 1:3, 1:4, and 1:5, respectively, and magnetically stirred at 400 rpm and 25 °C for 30 min to obtain homogeneous CNFs/LNPs suspensions. For each mass ratio, three independent CNFs/LNPs suspensions were prepared and measured separately. All suspensions used for subsequent measurements were diluted to 0.1 wt% with distilled water. The zeta potential of the CNFs/LNPs complexes and the hydrodynamic particle size of LNPs were measured at 25 °C using a Zetasizer Nano ZS90 (Malvern Instruments Ltd., UK) as described (Zhao et al., 2026). The particle-size distributions of the CNFs/LNPs complexes were measured using a Mastersizer 2000 laser diffraction particle size analyzer (Malvern Instruments Ltd., UK).

2.3.5. Morphological characterization of CNFs/LNPs complexes

The CNFs/LNPs complex with a mass ratio of 1:3 was selected for morphological characterization. The suspension was diluted to 0.04 wt % with distilled water, dried at 25 °C, and subsequently examined by a scanning electron microscope (SEM, MIRA LMS, TESCAN, Czech Republic) at an acceleration voltage of 5 kV.

2.4. Preparation of composite films

The composite films were prepared using solution casting method (Xiao et al., 2022). The film-forming solutions were prepared by mixing specified amounts of PVA solution (10 wt%), CNFs or eCNFs suspensions, LNPs suspension, ε-PL, and glycerol with distilled water. The detailed formulations and sample designations were summarized (Table S1-S3). The CNFs and LNPs loading percentages were calculated relative to the dry PVA mass, while glycerol was added at 30 wt% of the combined dry mass of PVA, CNFs/eCNFs, ε-PL, and LNPs. The well-mixed samples were stirred magnetically under 400 rpm at 25 °C for 30 min, and about 13 g of each film-forming solution was poured into a cylindrical mold (diameter: 9 cm; height: 1 cm). The samples were dried in a hot-air oven (DNG-9031A, Shanghai Jinghong Laboratory Instrument Co., Ltd., Shanghai, China) at 60 °C for 6 h, and the dried films were finally peeled off and conditioned at 25 ± 1 °C and 53 ± 2% relative humidity for 48 h.

2.5. Morphological observation, thickness and color measurements of composite films

The micro-morphology of film sample was characterized by SEM at an acceleration voltage of 5 kV. The films were subjected to brittle fracture in liquid nitrogen, and the surface and cross-section were coated with gold. The thickness of the films was determined by measuring ten randomly-selected points on each sample using a digital micrometer (CH-1-S, Shanghai Liu-ling Instrument Company, China). The surface color of the films was determined using a colorimeter (WF-28, Shenzhen Weifu Optoelectronic Technology Co., Ltd., China) as described (Haghighi et al., 2021). The color parameters, including L* (lightness), a*(red/green), and b* (yellow/blue), were recorded, and total color difference (ΔE) was acquired via the eq. (5):

$$\Delta E = \sqrt{(L^* - L_0)^2 + (a^* - a_0)^2 + (b^* - b_0)^2} \quad (5)$$

Where L*, a*, and b* are the color parameters of the film samples, while L_0, a_0, and b_0 represent the values of the white standard plate ($L_0 = 92.45$, $a_0 = -0.69$, $b_0 = -4.14$).

2.6. Physical and chemical characterizations of composite films

2.6.1. Fourier-transform infrared spectroscopy (FTIR) and X-ray photoelectron spectroscopy (XPS)

Spectra of PVA, CNFs, LNPs, ε-PL, and blend films were respectively recorded using an FTIR spectrometer (Nicolet iN10, Thermo Fisher Scientific, USA) at 25 °C. Data were collected in the range of 4000 to 400 cm^{-1} with a resolution of 4 cm^{-1} and 32 scans (Xiao et al., 2022). X-ray photoelectron spectrometer (ESCALAB Xi+, Thermo Fisher, USA) was employed to analyze surface elemental composition of the blend films (Pei et al., 2025). The samples were positioned perpendicular to the X-ray source for analysis. Data acquisition was performed based on the specific elements of interest, and the obtained spectra were processed using Avantage software (v5.992).

2.6.2. Thermogravimetric (TG)

Thermal stability of the films was evaluated using a thermogravimetric analyzer (TGA, Discovery 5500, TA Instruments, USA). Approximately 5 mg film sample was placed in a ceramic pan, and the detection was performed in a temperature range of 25 °C to 600 °C at a heating rate of 10 °C/min under a nitrogen atmosphere with a flow rate of 30 mL/min (Han et al., 2025). The onset decomposition temperature (T_{onset}) was determined by the extrapolated tangent-intersection method from the TG curve (Li et al., 2023; Peng et al., 2025). The maximum degradation temperature (T_{max}) was defined as the temperature corresponding to the maximum mass-loss rate in the derivative thermogravimetric (DTG) curve. Char yield was determined as the residual mass percentage at 600 °C.

2.6.3. Water resistance and barrier properties

The water solubility and swelling ratio of the composite films were respectively measured as described (Xiang et al., 2021). Water vapor permeability (WVP) was determined according to the method of Mai et al. (2023) with minor modifications. About 3 g of calcium sulfate was placed in an amber vial with an opening diameter of 2 cm to maintain a relative humidity of 0% inside the vial. The opening of the container was completely covered and tightly sealed with the film sample. All sample bottles were placed in a desiccator containing potassium sulfate and maintained at 25 °C for 48 h under a relative humidity of 97 ± 2%. The mass of each vial was recorded at 24 h intervals. WVP was calculated using the following eq. (6):

$$WVP = \frac{(m - m_0) \times d}{t \times s \times \Delta P} \quad (6)$$

Where m and m_0 are the mass (g) of the vial at time t and its initial mass, respectively; d is the actual thickness measured for the corresponding film sample; t is the permeation time; s is the effective permeation area; and ΔP is the water vapor partial pressure difference across the film at 25 °C. WVP was expressed as 10^{-14}·g·cm^{-1}·s^{-1}·Pa^{-1}.

Oxygen transmission rate (OTR) was determined using an oxygen-scavenger adsorption method (Zhang et al., 2016). Briefly, 3.0 g of an oxygen-scavenging mixture consisting of sodium chloride, reduced iron powder, and activated carbon at a mass ratio of 1.5:0.5:1 was placed in an amber vial with an opening diameter of 2 cm. The opening of the container was completely covered and tightly sealed with the film sample. All sample bottles were placed in a desiccator containing barium chloride and maintained at 25 °C for 48 h under a relative humidity of 90 ± 2%. The oxygen transmission rate was calculated using the following eq. (7):

$$OTR = \frac{m - m_0}{t \times s} \quad (7)$$

Where m and m_0 are the mass (g) of the container after exposure for time t and its initial mass, respectively; t is the permeation time (h); and s is the effective permeation area (m^2). OTR was expressed as g·h^{-1}·m^{-2}.

2.6.4. UV-blocking measurements

The UV-blocking performance of the composite films was measured using a UV–Vis spectrophotometer (T600, Beijing Purkinje General Instrument Co., Ltd., China). Rectangular film samples (4 cm × 2 cm) were cut and attached to the test cell to ensure a flat and tight fit. The spectra were scanned in the wavelength range of 200–800 nm. The visible light transmittance of the composite films at 600 nm (T_{600}) was directly obtained from the corresponding UV–Vis transmittance spectra (Guzman-

Puyol et al., 2022). The UVA and UVB blocking percentages were calculated from the spectral transmittance data according to Wei et al. (2024). Transmittance (T) was collected at 1 nm intervals over the UVA (320–400 nm) and UVB (280–320 nm) regions.

The UVA (320–400 nm) blocking percentage was calculated using the following eq. (8):

$$UVA\ blocking\ (\%) = 100 - \frac{\int_{320}^{400} T(\lambda)d\lambda}{\int_{320}^{400} d\lambda}(\%) \quad (8)$$

The UVB (280–320 nm) blocking percentage was calculated using the following eq. (9):

$$UVB\ blocking\ (\%) = 100 - \frac{\int_{280}^{320} T(\lambda)d\lambda}{\int_{280}^{320} d\lambda}(\%) \quad (9)$$

Where T(λ) is the average spectral transmittance of the composite film, dλ is the bandwidth and λ is the wavelength.

2.7. Mechanical detection of composite films

The tensile strength (TS) and elongation at break (EAB) of the films were determined using a texture analyzer (TA.XT Plus, Stable Micro Systems, UK) according to the ASTM standard method D882–91 (ASTM, 1996) and Wu et al. (2023). Film samples were cut into strips with a total length of 50 mm and a width of 10 mm. The initial distance between the grips (gauge length, L_0) was set at 30 mm, with 10 mm at each end of the sample clamped by the grips. Tensile tests were performed at a cross-head speed of 0.5 mm/s with a trigger force of 5.0 g. The thickness (T) used for stress calculation was the actual thickness measured for the corresponding film sample. TS and EAB were calculated according to eqs. (10) and (11), respectively:

$$TS = \frac{F}{T \times W} \quad (10)$$

$$EAB = \frac{(L - L_0)}{L_0} \times 100\% \quad (11)$$

Where F is the maximum force (N), T and W are the thickness (mm) and width (mm) of the film strip, respectively. L_0 is the initial length of the film strip between grips, and L is the final length at the point of film strip breakage.

To evaluate the durability of the films after exposures of extreme temperatures, the mechanical properties were re-examined after the samples were exposed to 100 °C for up to 3 h using a drying oven (DNG-9031 A, Shanghai Jinghong Laboratory Instrument Co., Ltd., Shanghai, China) or stored at −80 °C for up to 150 days in a freezer (DW-86 L626, Haier Biomedical Co., Ltd., Qingdao, China). At the designated treatment times, the samples were removed from the oven or freezer and immediately tested at room temperature under the conditions described above.

2.8. Antioxidant activity assay of composite films

The DMSO-extractable radical-scavenging activity of the films was evaluated using the 2,2-diphenyl-1-picrylhydrazyl (DPPH) radical scavenging assay as described (He et al., 2023). About 50 mg film sample was immersed in 10 mL dimethyl sulfoxide (DMSO) and kept under dark at room temperature for 24 h. The extract was centrifuged at 3000 *g* for 5 min, and about 0.5 mL of each supernatant was removed and mixed uniformly with 3.5 mL of 0.2 mM DPPH (dissolved in ethanol). The mixed sample was incubated under dark at room temperature for 30 min. The absorbance was measured at 517 nm, and a mixture of 0.5 mL DMSO and 3.5 mL DPPH solution was used as the control. The DPPH radical-scavenging activity was calculated regarding the eq. (12):

$$\text{DPPH radical scavenging activity}\ (\%) = \left[1 - \frac{(A_s - A_b)}{A_0}\right] \times 100 \quad (12)$$

where A_0 is the absorbance of the mixture containing 0.5 mL of DMSO and 3.5 mL of DPPH solution, A_s is the absorbance of the mixture containing 0.5 mL of sample supernatant and 3.5 mL of DPPH solution, and A_b is the absorbance of the mixture containing 0.5 mL of sample supernatant and 3.5 mL of ethanol.

2.9. Evaluation of cherry tomatoes preservation

Cherry tomatoes with consistent ripeness and dimensions were selected and loaded into 600 mL commercial plastic containers (140 mm diameter). The plastic containers were capped with the prepared composite films or PE cling film. To ensure a tight seal, the films were immobilized using double-sided tape. All samples were stored in a climate-controlled chamber at 26 ± 1 °C with 37 ± 1% relative humidity for 10 days, and their quality evolution was analyzed. The weight loss was determined by monitoring the changes in the mass of the cherry tomatoes throughout the storage period regarding the eq. (13):

$$\text{Weight loss}\ (\%) = \frac{m_0 - m_\chi}{m_0} \times 100 \quad (13)$$

Where m_0 represents the initial weight of the fruit (Day 0), and m_χ represents the weight measured at a specific storage interval.

The decay rate was evaluated through visual inspection. Fruits exhibiting any signs of visible mold growth, surface lesions, softening were evaluated as decayed. The decay rate was calculated separately for each container using the eq. (14) (Yu et al., 2023):

$$\text{Decay rate}\ (\%) = \frac{M_\chi}{M_0} \times 100 \quad (14)$$

Where M_χ represents the number of decayed fruits, and M_0 is the total number of fruits in the corresponding container with 18 fresh fruits.

Fruit firmness was determined using a texture analyzer (TA. XT Plus, Stable Micro System, UK) equipped with a P/2 probe (Xiao et al., 2022). A puncture test was performed by penetrating cherry tomato to a depth of 2 mm at a speed of 1.00 mm/s. The firmness was calculated as the maximum force per unit area (N/mm^2). The fruit extract was prepared by homogenizing 35 g cherry tomato samples (including peel and pulp) with 65 mL boiled reverse osmosis water (cooled to 25 °C), followed by filtration. The entire procedure was conducted under light-protected conditions to prevent oxidation. Using the obtained filtrate, total soluble solids (TSS) were measured in °Brix by placing an aliquot (>2 drops) onto a digital Abbe refractometer (WAY—2S, Shanghai Jingke Industrial Co., Ltd., China), whereas the pH value was determined using a digital pH meter (DELTA 320, Mettler-Toledo Instruments, Shanghai, China). The Vitamin C (Vc) content was analyzed as described (Chen et al., 2023).

All packaging groups and the control consisted of three independent containers, with 18 cherry tomatoes per container (54 fruits per treatment). The decay rate was calculated separately for each container using all 18 fruits, whereas the other quality parameters were measured using one fruit selected from each container at each sampling time point. Data were expressed as mean ± SD ($n = 3$ independent containers per group).

2.10. Statistical analysis

All experiments were conducted with independent replicates as indicated in the figure/table legends. Statistical analysis and figure drawing were conducted using Origin 2021 (Origin Lab Corporation, Northampton, MA). One-way analysis of variance (ANOVA) followed by Tukey's multiple range test was used for comparisons among multiple groups, while Student's *t*-test (**$p < 0.01$, *$p < 0.05$) was used for

comparisons between two groups.

3. Results and discussion

3.1. Distinct cellulose nanofibers assembly via enzymatic tailoring

As described in Fig. 1a & b, this study initially selected two *Miscanthus* accessions (Msa10, Msa32) distinctive at cell wall composition (Fig. S2). As a comparison, the Msa32 accession contained significantly higher cellulose (42%) and hemicellulose (25%) contents than Msa10 (35% and 21%), whereas Msa10 showed a higher lignin content (27%) than Msa32 (24%). Since both *Miscanthus* accessions accumulate much cellulose in mature straws, this work prepared the CNFs by chemical removals of lignin and hemicellulose from mature *Miscanthus* straws followed with ball milling and high-pressure homogenization treatments with the remaining cellulose microfibrils (Fig. S1). Because the CNFs were defined by the amorphous/defect regions on the surfaces of cellulose microfibrils accountable for the breakpoints for initiation of enzymatic digestion (Ai et al., 2024; Peng et al., 2022; Zhang, Hu, Peng, et al., 2023; Zhang, Hu, Wang, et al., 2023), this study further modified CNFs by incubation with mixed-cellulase for a short time (Fig. S3), and the resulting eCNFs remained more than 70% of total cellulose substrates after incubations for 1–2 h (Table S4). The chemical compositions of the resulting CNFs and eCNFs were further characterized, with eCNFs obtained by enzymatic hydrolysis of CNFs for 1 h (Table S5). After enzymatic hydrolysis, the hemicellulose fraction decreased significantly from 8.75% to 6.05% in Msa10 and from 8.06% to 6.88% in Msa32, whereas the cellulose and lignin fractions showed no significant differences (Table S5). These results indicated that enzymatic digestion altered the residual polysaccharide composition in addition to fibril morphology and cellulose DP. By means of our previously-established atomic force microscopy (AFM) approach, we characterized the surface topography of CNFs and eCNFs by measuring the distances between adjacent surface defects in two *Miscanthus* accessions (Fig. 2a & b; Fig. S4). As a result, the inter-defect distances of CNFs and eCNFs from Msa32 were significantly shorter than those of Msa10 by 48% and 26%, at $p < 0.05$ levels ($n = 50$), whereas the inter-defect distances of eCNFs of two *Miscanthus* samples were significantly reduced by 58% and 39% relative to their CNFs ones, indicating that eCNFs of Msa32 exhibited the shortest inter-defect distance of 24.86 nm (Table S6). Furthermore, we measured the average apparent widths and local height differences of two defects, and eCNFs(Msa32) exhibited the lowest values of both parameters (Fig. 2c-e; Table S6). The AFM-measured apparent lateral fibril widths ranged from 32.91 to 67.24 nm (Fig. 2f; Table S6), exceeding the TEM-derived fibril diameters of 2.56–5.21 nm (Fig. S5). Compared with the corresponding Msa10 samples, Msa32 had significantly lower cellulose DP of CFs, CNFs, and eCNFs (Fig. 2g), with the greatest relative reduction (37%) for CFs. These differences were accompanied by smaller apparent lateral fibril widths and shorter inter-defect distances in Msa32-derived samples. The corresponding estimated molecular weight (M) derived from cellulose DP was summarized in Table S7, showing a consistent decrease after enzymatic hydrolysis. Further comparisons confirmed that both CNFs(Msa32) and eCNFs (Msa32) exhibited significantly lower estimated molecular weights than their corresponding Msa10 samples ($p < 0.01$), with eCNFs(Msa32) showing the lowest value of 33.56 kDa (Table S7). Therefore, this study demonstrated that the enzymatic tailoring could alter both CNFs morphology and composition, as reflected by changes in apparent fibril dimensions, shorter inter-defect distances, reduced cellulose DP values, and less residual hemicellulose fractions.

3.2. Interfacial association between CNFs and LNPs

Based on the enzymatically-induced CNFs changes described above,

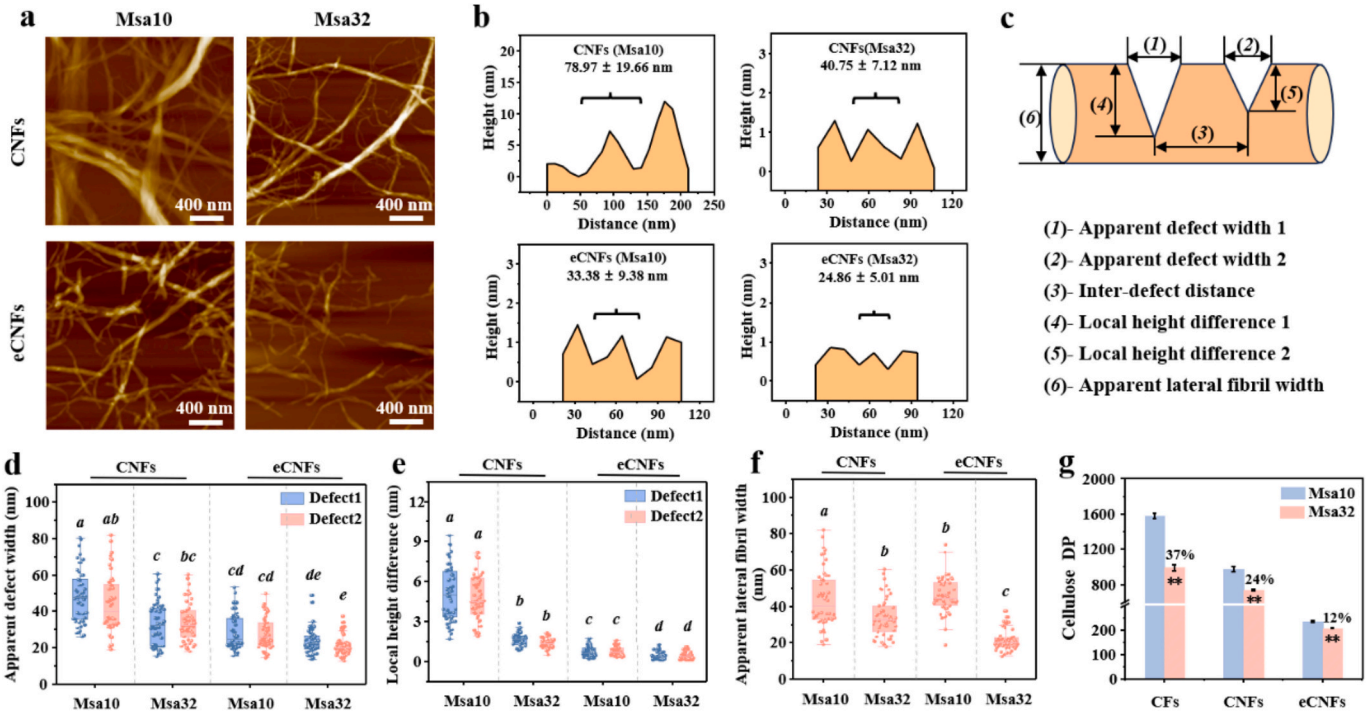


Fig. 2. Characterization of CNFs and eCNFs derived from two *Miscanthus* accessions (Msa10, Msa32). (a) AFM images. (b) Inter-defect distances. (c) Schematic representation of CNFs with surface defects. (d, e) Apparent defect widths and local height differences, respectively. (f) AFM-derived apparent lateral fibril widths. AFM data as mean ± SD ($n = 50$ technical measurements from one representative preparation per sample). Different lowercase letters as significant differences ($p < 0.05$, one-way ANOVA followed by Tukey's multiple range test), based on separated eight-group comparisons for (d) and (e) and four-group comparisons for (b) and (f). The eCNFs obtained after 1 h of enzymatic hydrolysis. (g) Cellulose degree of polymerization (DP). Data as mean ± SD from three independent sample preparations ($n = 3$). ** As significant difference between Msa10 and Msa32 within the corresponding sample type ($p < 0.01$, Student's *t*-test).

we further investigated the interfacial association between CNFs/eCNFs and LNPs (Fig. 1c-d). By employing the alkaline lignin containing high proportions of G- and S-monomers (Table S8), the ultrasonication-assistant LNPs with TEM diameters mainly distributed between 7 nm and 25 nm with average diameter of 16.77 nm (Fig. 3a). As LNPs sizes were measured by TEM, it should explain why AFM-measured defects of eCNFs could not precisely match for appropriate-size LNPs association. In contrast, DLS measurements showed an average hydrodynamic diameter of 140.43 nm and a PDI of 0.39 (Fig. S6a), reflecting differences between dried-state TEM observations and dispersion-state measurements, potentially including particle aggregation. The CNFs and eCNFs of two *Miscanthus* accessions (Msa10, Msa32) were then combined with LNPs to examine their morphological association (Fig. 3b). To screen the CNFs/LNPs mixing ratios, we detected the zeta potentials of various CNFs/LNPs dispersions at dry-mass ratios of 1:1 to 1:5 proportions (Table S9). The 1:3 mixtures exhibited the most negative average zeta potentials within the mixed series (−16.20 mV for Msa10 and − 18.13 mV for Msa32), although their values were not statistically distinct from 1:4 mixtures and 1:5 mixtures. Laser-diffraction measurements further showed that the 1:3 mixtures had the lowest volume-weighted diameters ($D_{4,3}$ = 16.50 μm for Msa10 and 13.55 μm for Msa32) and Span values (1.64 and 1.33) among the tested ratios (Fig. S6b, c; Table S10). These results thus supported the selection of the 1:3 mass ratio for further experiments based on the comparatively smaller and narrower aggregate size distributions. Using the selected 1:3 mass ratio, we observed more pronounced apparent thickening and particle association around CNFs/eCNFs in the Msa32-derived samples than in the Msa10-derived samples (Fig. 3b). These morphological features were consistent with possible CNFs/LNPs interfacial association and packing, potentially influenced by the structural and compositional differences of enzymatically-tailored eCNFs.

3.3. Construction of characteristic PVA/CNFs/ε-PL/LNPs films

3.3.1. Optimization of CNFs loading in PVA films

To construct PVA/CNFs/ε-PL/LNPs composite films, this study first examined the incorporation of different CNFs loadings into the PVA matrix. By supplying different masses of CNFs and glycerol into PVA, we observed that the thicknesses of PVA/CNFs films increased with CNFs loading, whereas the control film (PVA only) was of 46 μm (Fig. S7a; Table S1). The increased thicknesses of PVA/CNFs film were mainly associated with the increased solid content. Notably, both water vapor permeability (WVP) and oxygen transmission rate (OTR) reached their lowest values at 5% CNFs loading in the Msa10 and Msa32 films (Fig. S7b & c). The reduction in WVP was consistent with a more tortuous diffusion pathway, in which dispersed CNFs may hinder water vapor transport through the PVA matrix (Xiang et al., 2021). Meanwhile, the OTR values exhibited a similar decreasing trend, suggesting improved oxygen-barrier performance under the test conditions. At CNFs loadings exceeding 5%, both WVP and OTR increased, potentially due to less homogeneous fibril dispersion and packing, which may introduce less resistant transport pathways (Trigui et al., 2025). The mechanical properties of the PVA/CNFs films also varied with CNFs loading. The 5% CNFs loading achieved the highest tensile strength (TS) among the tested formulations for both Msa10 and Msa32 (Fig. S7d). This reinforcement may be associated with a physical network formed through hydrogen bonding and fibril entanglement within the PVA matrix (Wang et al., 2018). On the other hand, CNFs loadings exceeding 5% resulted in reduced tensile strength, potentially owing to fibril aggregation and less effective stress transfer. Similarly, among the CNFs-containing formulations, the 5% CNFs films exhibited the highest elongation at break (EAB) (Fig. S7e). Collectively, these results supported the 5% CNFs selection for subsequent composite film preparation based on the balance of barrier and mechanical properties.

3.3.2. Morphology and interfacial association of PVA/CNFs/ε-PL/LNPs films

Based on the selected 5% CNFs loading, this study constructed various PVA/CNFs/ε-PL/LNPs films by incorporating different amounts of LNPs and glycerol along with 5% CNFs and ε-PL (Table S2 & S3). As a result, all composite films exhibited relatively smooth surfaces without obvious cracks, particularly those containing 15% LNPs (Fig. 4a), suggesting a component compatibility. Compared with the Msa10-based films, the Msa32-based films exhibited more uniform and compact cross-sections, while the eCNFs-containing films showed relatively denser morphologies than their CNFs-containing counterparts. In particular, the Msa32-derived eCNFs film exhibited a compact morphology, consistent with possible differences in component packing and physical association. Furthermore, FTIR spectra revealed changes in the characteristic absorption bands of the constituent materials after film formation (Fig. 4b & c; Fig. S8). For example, the absorption peak in the range of 3200–3500 cm^{-1} became broader after integration, being accountable for the possible hydrogen-bonding interactions among PVA, CNFs/eCNFs, ε-PL, and LNPs. Changes around 1550–1560 cm^{-1} may include contributions from ε-PL-associated vibrations. XPS assay was also performed to observe the high-resolution spectra of surface chemical compositions in the composite films (Fig. 4d-f; Fig. S9). For the C 1 s spectra, the main peaks assigned to C—C, C-O-C, and O-C=O indicated the presence of carbon species from CNFs/eCNFs, PVA, LNPs and ε-PL, whereas the fitted peaks corresponding to C=O, C—O and adsorbed oxygen confirmed the existence of abundant oxygen-containing groups in the O 1 s spectra. The N 1 s peak located at 399.5–399.8 eV was

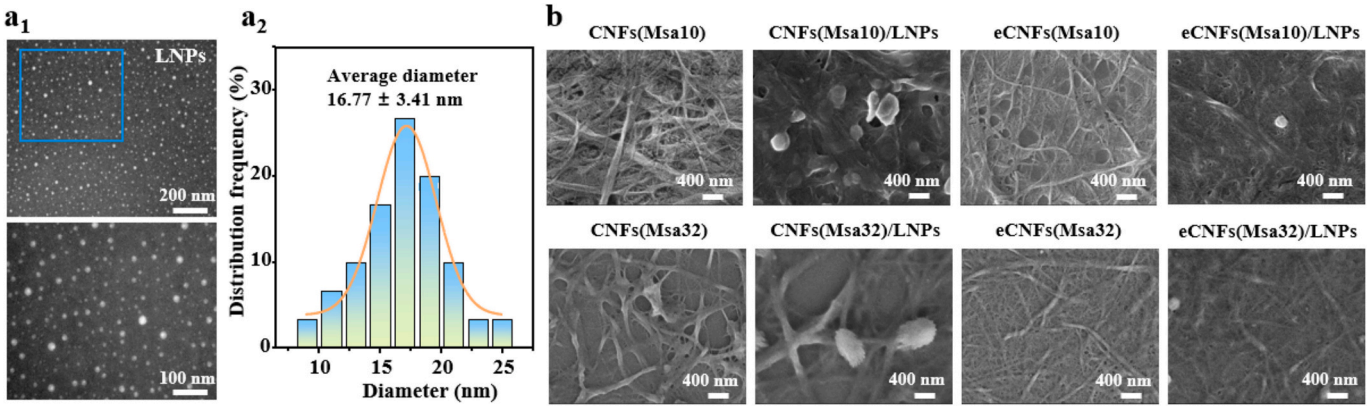


Fig. 3. Morphological characterization of LNPs and CNFs/LNPs complexes. (a_1) TEM images of LNPs generated from alkali lignin. (a_2) Particle diameter distribution of LNPs. (b) SEM images of CNFs/eCNFs and their corresponding CNFs/LNPs complex prepared at 1:3 mass ratio. TEM particle diameters as mean ± SD (n = 30 technical measurements from one representative image).

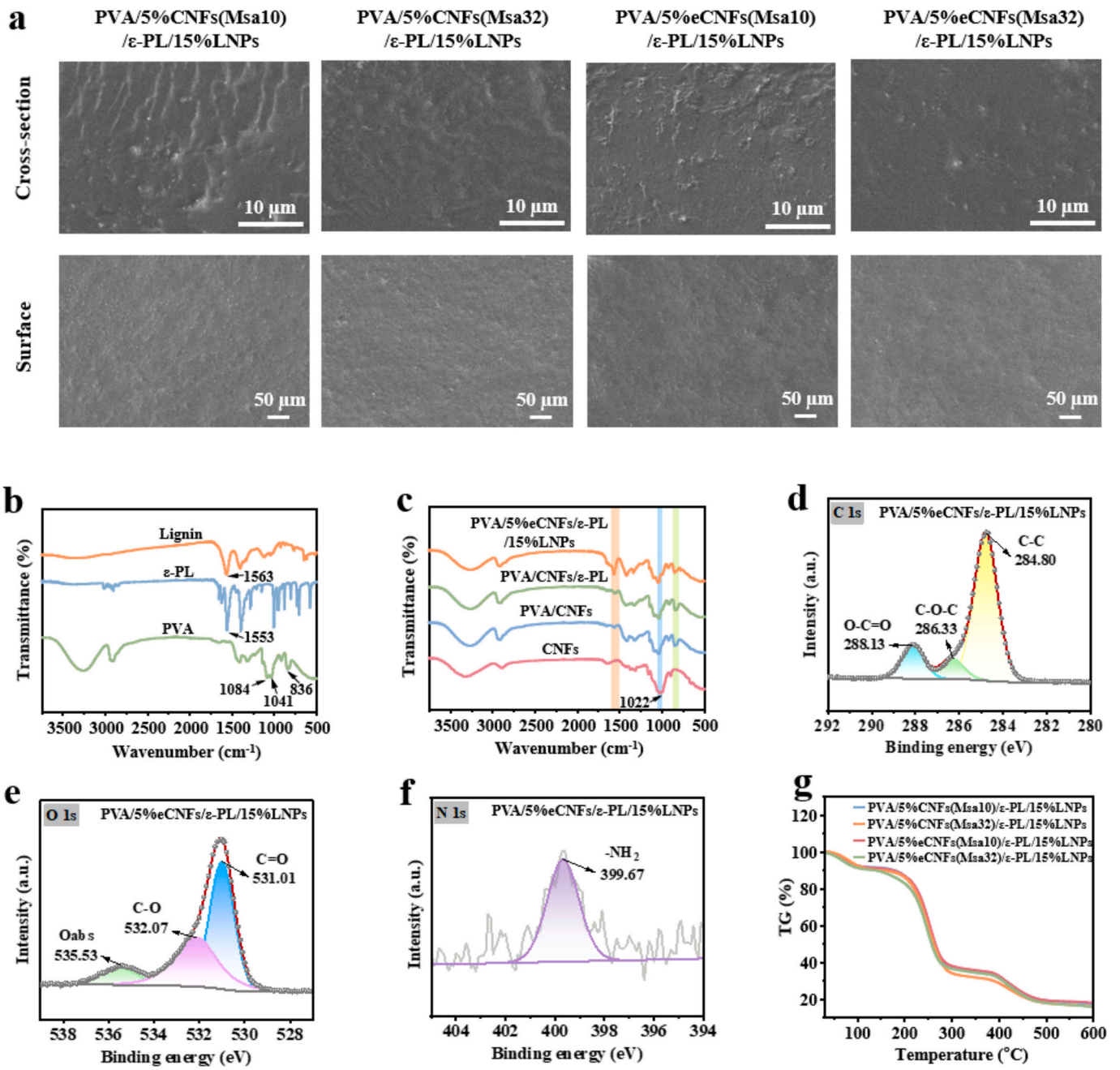


Fig. 4. Characterization of the composite films of two *Miscanthus* accessions (Msa10, Msa32). (a) SEM images of surface and cross-section. (b & c) FT-IR spectra of Msa32-based samples. (d-f) High-resolution spectra of XPS of Msa32-based samples. (g) TG curves.

assigned to amino groups, being accountable for incorporation of ε-PL into the film matrix. Overall, the FTIR and XPS observations both supported a possible physical association among the film components.

3.3.3. *Thermal stability of PVA/CNFs/ε-PL/LNPs films*

The thermal stability of the composite films was also evaluated by TG and DTG profiling (Fig. 4g; Fig. S10). In general, the four films of two *Miscanthus* accessions exhibited a similar thermal decomposition pattern under the temperatures ranged from 30 °C to 600 °C. In particular, all films presented four stages of weight loss: The first stage (30 °C - 150 °C) showed a slight weight loss, mainly due to the volatilization of free water in the films; The second stage (150 °C - 230 °C) had a slow weight loss, which was mainly attributed to the removal of bound water and glycerol; The third stage (230 °C - 300 °C) showed a drastic loss, which should be mainly due to the thermal decomposition of PVA and CNFs and the degradation of ε-PL and LNPs; The fourth stage (350 °C - 500 °C) should involve in further decomposition of lignin-derived aromatic structures and carbonaceous residues in the composite films. Despite the structural differences between CNFs and eCNFs, the four composite films exhibited relatively small variations in T_{onset}, T_{max}, and char yield (Table S11), indicating generally comparable thermal stability.

3.4. *Physical and barrier properties of PVA/CNFs/ε-PL/LNPs films*

With regards to the diverse PVA/CNFs/ε-PL/LNPs films, this study compared their color difference via a ΔE assay (Fig. 5a-c). As LNPs loading was increasing, the ΔE values gradually raised (Fig. 5b). At fixed eCNFs and LNPs loadings of 5% and 15%, the ΔE values increased slightly after 1 h enzymatic hydrolysis, but decreased after 2 h hydrolysis (Fig. 5c). The Msa32-based films generally exhibited higher ΔE

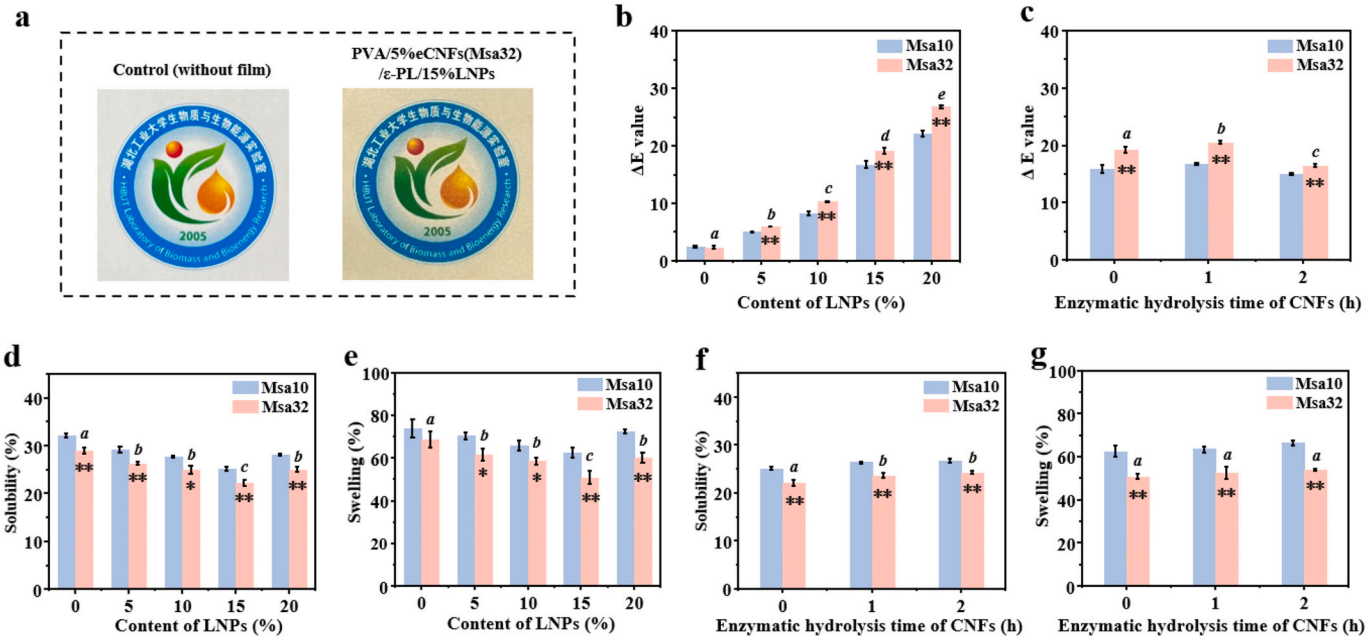


Fig. 5. Comparison of physical properties of the PVA/5%CNFs/ε-PL/LNPs films derived from two *Miscanthus* accessions (Msa10, Msa32). (a) Visual photographs of the selected film containing eCNFs obtained after 1 h of enzymatic hydrolysis and the control. (b) Color difference (ΔE) values of the 5% CNFs-based films containing different LNPs loadings. (c) ΔE values of films containing 15% LNPs and 5% CNFs/eCNFs obtained after 0–2 h of enzymatic hydrolyses. (d & e) Solubility and swelling values of the films shown in (b). (f & g) Solubility and swelling values of the films shown in (c). Data as mean ± SD ($n = 3$). Different lowercase letters as significant differences among the Msa32 formulations ($p < 0.05$). * And ** as significant differences between the corresponding Msa10 and Msa32 formulations at $p < 0.05$ and $p < 0.01$, respectively.

values than the corresponding Msa10-based films, indicating greater color differences. Likewise, the film thickness increased with LNPs loading, whereas relatively smaller differences were observed between the corresponding *Miscanthus* accessions and CNFs/eCNFs formulations (Fig. S11). As major water-resistance properties, the solubility and swelling of all PVA/5%CNFs/ε-PL/LNPs and PVA/5%eCNFs/ε-PL/LNPs films were detected in this study (Fig. 5d-g). Increasing LNPs loading to 15% could progressively reduce the film solubility and swelling in both

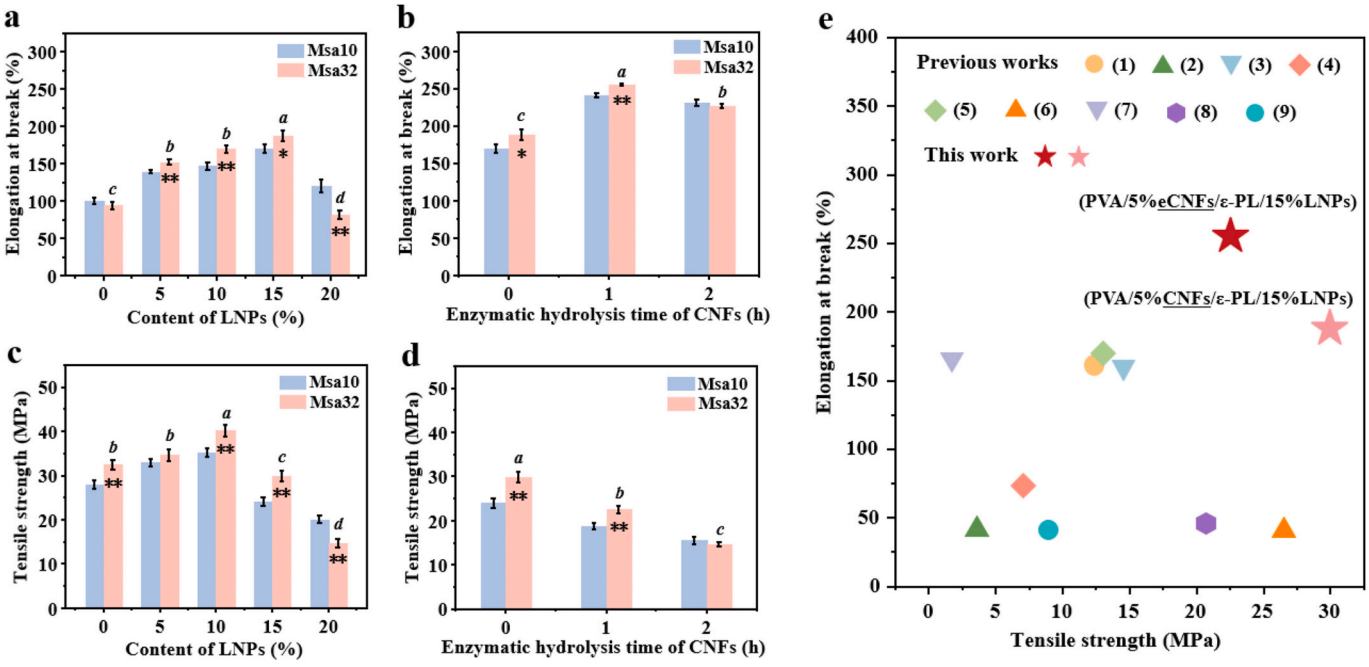


Fig. 6. Comparison of mechanical properties of the PVA/CNFs/ε-PL/LNPs composite films derived from two *Miscanthus* accessions (Msa10, Msa32). (a & b) Elongation at break (EAB) of the film samples corresponding to the formulations shown in Fig. 5b and c, respectively. (c & d) Tensile strength (TS) of the corresponding films. (e) Contextual comparison of the two Msa32-based films containing 15% LNPs with the other films comprising cellulose or lignin as selected from the previous studies 1–9 and their detailed information as shown in Table S13. Data in (a-d) as mean ± SD from three independently cast films for each formulation ($n = 3$ independent films). Different lowercase letters as significant differences among the Msa32 formulations ($p < 0.05$). * And ** as significant differences between the corresponding Msa10 and Msa32 formulations at $p < 0.05$ and $p < 0.01$, respectively.

Miscanthus accessions with the lowest values observed at 15% LNPs (Fig. 5d & e). But, further increasing LNPs loading to 20% adversely increased both values, probably owing to less homogeneous LNPs dispersion at higher loadings. The Msa32-based films generally showed lower solubility and swelling than their Msa10 counterparts, indicating comparatively improved water resistance. Meanwhile, the enzymatic hydrolysis of CNFs slightly increased the film solubility, but did not affect film swelling (Fig. 5f & g). These results thus identified 15% LNPs as a favorable loading for reducing film solubility and swelling.

Moreover, this study detected water vapor permeability (WVP) and oxygen transmission rate (OTR) of all films (Fig. S12). Both WVP and OTR decreased with LNPs incorporation, and reached their lowest values at 10% LNPs loading, followed with moderate increases at higher loadings (Fig. S12a & c). At a fixed 15% LNPs loading, enzymatically-tailored eCNFs caused relatively modest changes in WVP and OTR (Fig. S12b & d). In addition, the Msa32-based films generally had lower WVP and OTR values than the corresponding Msa10-based films. Although 10% LNPs provided the lowest WVP and OTR, 15% LNPs gave the lowest solubility and swelling values while maintaining relatively favorable barrier performance.

3.5. Mechanical properties of PVA/CNFs/ε-PL/LNPs films

To test mechanical performance of the desirable PVA/5%eCNFs/ε-PL/15%LNPs films, this study examined both elongation at break (EAB) and tensile strength (TS) of all films under room temperature (Fig. 6a-d), which are two critical parameters accounting for mechanic properties (Ning et al., 2025). As LNPs loading increased from 0% to 20%, EAB of films containing 5% CNFs initially increased and subsequently decreased, reaching a maximum of 187.84% for the Msa32-based film at 15% LNPs (Fig. 6a). At 15% LNPs loading, enzymatic hydrolysis of CNFs for 1 h further increased EAB to 240.67% and 255.30% for the Msa10- and Msa32-based films, respectively, whereas prolonged hydrolysis for 2 h resulted in lower EAB values (Fig. 6b). In contrast, TS reached its maximum of 40.18 MPa in the Msa32-based film containing 10% LNPs (Fig. 6c). At 15% LNPs, the corresponding CNFs-containing film exhibited a TS of 29.96 MPa, which decreased to 22.54 MPa after the incorporation of eCNFs obtained by 1 h of enzymatic hydrolysis (Fig. 6d). Although the 10% LNPs formulation was of the highest TS and lowest WVP and OTR values, the 15% LNPs formulation achieved the highest EAB among all LNPs-loading samples, together with the lowest solubility and swelling values and favorable barrier properties. Further increasing LNPs loading to 20% reduced EAB while increasing solubility and swelling. Therefore, 15% LNPs was selected to achieve a favorable balance among mechanical flexibility, tensile strength, water resistance, and barrier performance. In addition, the mechanical properties of the two Msa32-based films containing 15% LNPs were compared with those of films comprising cellulose or lignin as selected from the previous works (Fig. 6e; Table S13). The present films maintained a favorable combination of high extensibility and appreciable tensile strength among all selected literature examples. Overall, the PVA/5%CNFs/ε-PL/15%LNPs and PVA/5%eCNFs/ε-PL/15%LNPs films derived from Msa32 were selected as the overall balanced formulations for further multiple functions and specific applications.

3.6. Mechanical stability after extreme-temperature exposures

As the two selected films exhibited different EAB and TS values, this study evaluated their mechanical property and stability after exposure to extreme temperatures (Fig. 1f; Fig. 7). After 2.5 h of exposure at 100 °C, the PVA/5%eCNFs/ε-PL/15%LNPs film showed a smaller reduction in EAB, whereas the PVA/5%CNFs/ε-PL/15%LNPs film appeared an approximately linear decrease until EAB was close to the minimum value (Fig. 7b). Even though the PVA/5%CNFs/ε-PL/15%LNPs film had a higher TS than the corresponding eCNFs-containing film at room temperature as examined above, it had a marked TS reduction, being close to the PVA/5%eCNFs/ε-PL/15%LNPs film after short incubation for 0.5 h at 100 °C (Fig. 7c). After 3 h of exposure at 100 °C, the

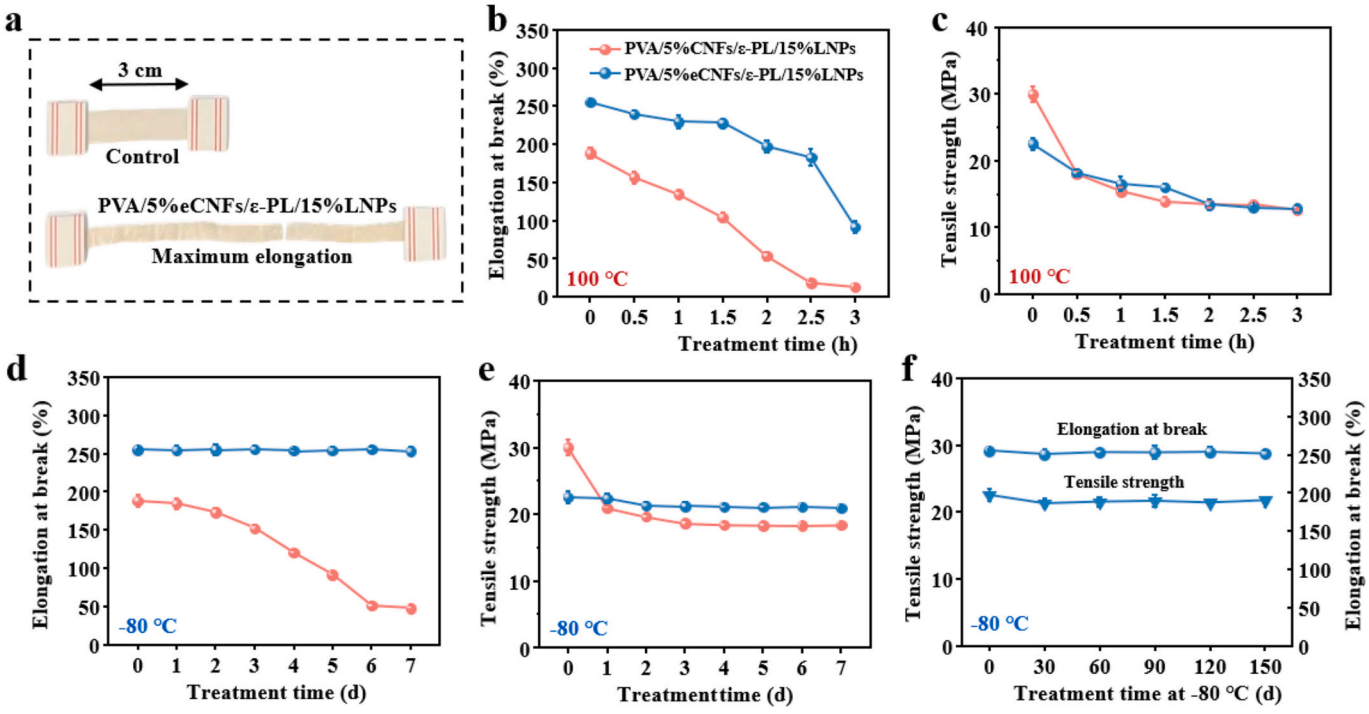


Fig. 7. Mechanical stability of the selected Msa32-based composite films after temperature treatments. (a) Visual photographs of the PVA/5%eCNFs/ε-PL/15%LNPs films before (control) and after tensile test (TS = 22.54 MPa, EAB = 255.30%). (b & c) EAB and TS after exposure to 100 °C for up to 3 h. (d & e) EAB and TS after storage at −80 °C for up to 7 days. (f) EAB and TS of the PVA/5%eCNFs/ε-PL/15%LNPs film after storage at −80 °C for up to 150 days. Data as mean ± SD (n = 3 independent films per time point).

PVA/5%eCNFs/ε-PL/15%LNPs film retained 56.79% of its initial TS and 35.81% of its initial EAB, whereas the PVA/5%CNFs/ε-PL/15%LNPs film showed 42.02% of its initial TS and 6.90% of its initial EAB, respectively (Fig. 7b & c). During 7-day storage at −80 °C, the PVA/5% eCNFs/ε-PL/15%LNPs film showed relatively stable EAB and TS, but the PVA/5%CNFs/ε-PL/15%LNPs film had a drastic reduction of EAB and consistently lower TS from one-day treatment (Fig. 7d & e). The PVA/5%eCNFs/ε-PL/15%LNPs film also maintained relatively stable EAB and TS during 150 days of storage at −80 °C, retaining 98.46% of its initial EAB and 96.58% of its initial TS after 150 days (Fig. 7f). Therefore, the results indicated that the selected PVA/5%eCNFs/ε-PL/15%LNPs film with maximum EAB could better retain its EAB after exposure to 100 °C or − 80 °C storage, whereas the PVA/5%CNFs/ε-PL/15%LNPs film had a greater reduction in EAB and TS after extreme temperature exposures.

3.7. UV-shielding and antioxidant performance

As lignin has been characterized with the functions against UV radiation and oxidative stress in plants (Yu et al., 2025), this study evaluated the UV-shielding and antioxidant properties of all composite films (Fig. 1f; Fig. 8). With increasing LNPs loading, all films showed enhanced UV shielding, with nearly complete UVC blocking observed at higher LNPs loadings in both *Miscanthus* accessions (Fig. 8a; Fig. S13a), which may be attributed to the phenolic hydroxyl groups and conjugated aromatic structures of LNPs.

At 15% LNPs loading, the UVA and UVB blocking percentages reached 83.86% and 97.46% for Msa10 and 87.86% and 98.52% for Msa32, respectively (Table S12). Consistently, the Msa32-based films generally exhibited higher UV-blocking percentages than those of the Msa10. Importantly, the PVA/5%eCNFs/ε-PL/15%LNPs film prepared using enzymatically-tailored CNFs(Msa32) for 1 h could maintain UVA and UVB blocking percentages of 87.14% and 98.34%, being comparable to those of the corresponding untreated CNFs(Msa32) films (Fig. 8b; Table S12). By contrast, the enzymatic hydrolysis of 5% CNFs(Msa32) for 2 h caused a decrease in UVA and UVB blocking percentages to 76.63% and 93.99% (Table S12). Despite the effective UV shielding, the films retained visible-light transmittance, with values at 600 nm of 65.72%, 52.22%, and 65.12% for the Msa32-based films containing untreated CNFs and eCNFs treated for 1 and 2 h, respectively (Table S12), potentially facilitating visual inspection of packaged food (Guzman-Puyol et al., 2022).

Furthermore, this study determined the DMSO-extractable DPPH radical scavenging capacity in two *Miscanthus* samples (Fig. 8c, d), providing an indicator of the radical scavenging capacity of extractable film components (Zhai et al., 2024). With raising LNPs loading, the DPPH radical scavenging activity increased in both Msa10 and Msa32

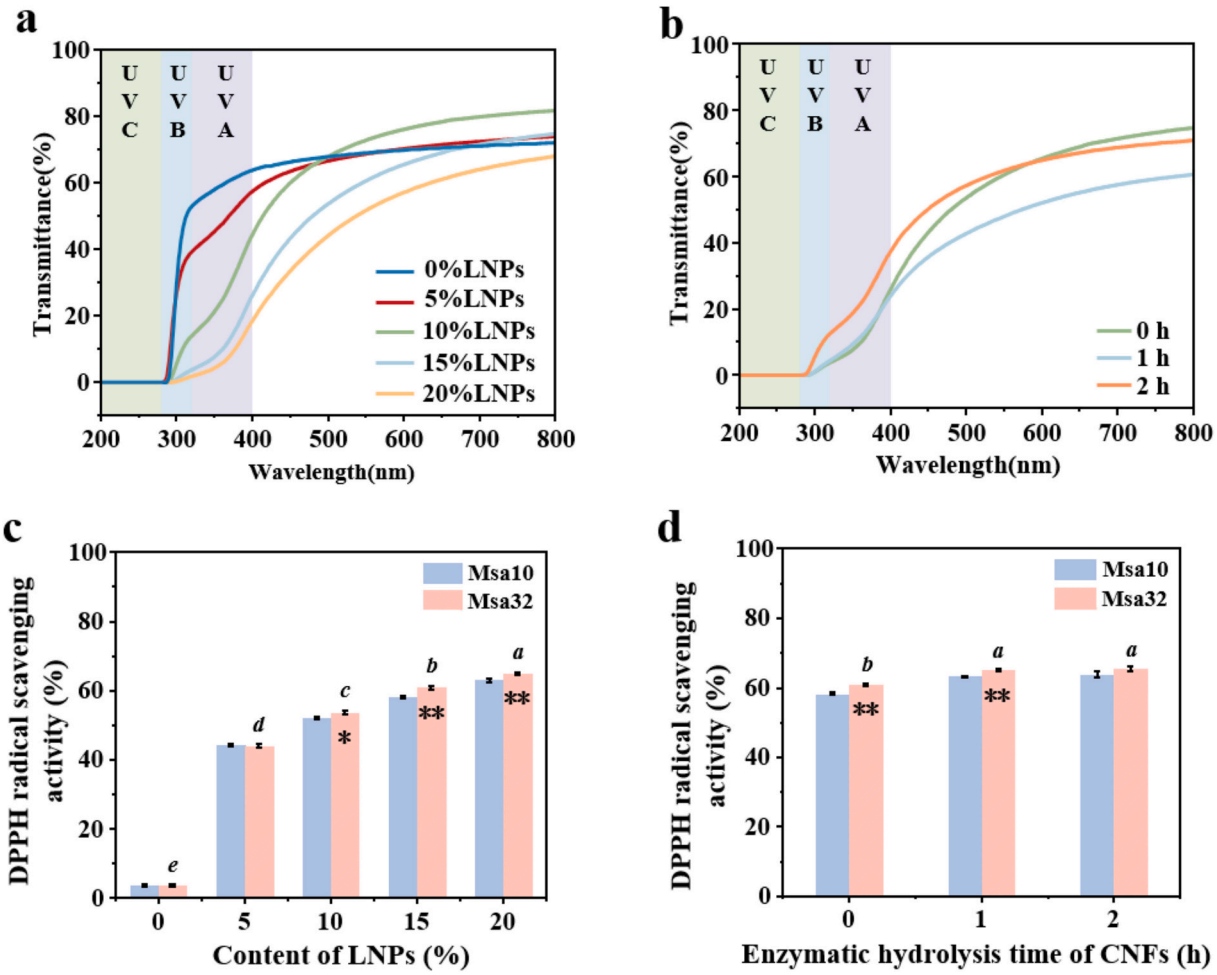


Fig. 8. UV-shielding and DMSO-extractable radical-scavenging properties of the composite films. (a) UV–Vis transmittance spectra of Msa32-derived PVA/5%CNFs/ε-PL/LNPs films with different LNPs loadings. (b) UV–Vis transmittance spectra of Msa32-derived PVA/5%eCNFs/ε-PL/15%LNPs films with different enzymatic hydrolysis times. (c, d) DPPH radical scavenging activity of DMSO extracts from the film samples corresponding to the formulations shown in Fig. 5b and c, respectively. DPPH data as mean ± SD from three independently cast films for each formulation ($n = 3$ independent films). Different lowercase letters as significant differences among the Msa32 formulations ($p < 0.05$). * And ** as significant differences between the corresponding Msa10 and Msa32 formulations at $p < 0.05$ and $p < 0.01$, respectively.

samples, indicating a contribution of LNPs to the extractable antioxidant activity. Likewise, the Msa32-based films generally had significantly higher DPPH radical-scavenging activity than the corresponding Msa10-based films at LNPs loadings of 10–20%, whereas no significant difference was detected at 5% LNPs loading. At a fixed 15% LNPs loading, enzymatic tailoring increased the DPPH radical scavenging activity of both *Miscanthus*-derived films, with relatively small changes between 1 and 2 h treatments (Fig. 8d). Therefore, the Msa32-derived PVA/5% eCNFs/ε-PL/15%LNPs film prepared using 1 h enzymatically-tailored CNFs was of strong UVA/UVB shielding and favorable DMSO-extractable radical scavenging activity.

3.8. Cherry tomato preservation performance

Because the comprehensive properties were improved in the selected PVA/5%eCNFs/ε-PL/15%LNPs film derived from Msa32, such as mechanical features, water vapor and oxygen barrier performances, water resistance, UV-shielding ability, and antioxidant activity, this study further evaluated its overall packaging performance using fresh cherry tomatoes during 10-day storage at room temperature (Fig. 1f; Fig. 9). As a result, the control samples (without film packaging) exhibited shriveling and decay after 10-day storage, whereas the polyethylene (PE) packaged samples started to exhibit apparent decay, mold growth and skin cracking at the eighth day with pronounced deterioration after 10-day storage (Fig. 9a). In contrast, the cherry tomatoes packaged with the PVA/5%CNFs/ε-PL/15%LNPs film only exhibited slight deterioration, whereas those packaged with the PVA/5%eCNFs/ε-PL/15%LNPs film retained generally fresh and smooth appearances after 10-day storage. To confirm those observations, this study measured the decay rates of cherry tomatoes during 10-day storage (Fig. 9b). As a comparison, the cherry tomatoes wrapped with the PVA/5%eCNFs/ε-PL/15%LNPs and PVA/5%CNFs/ε-PL/15%LNPs films showed average decay rates of 4% and 17% after 10-day storage, whereas the control and PE samples had the decay rates of 80% and 61%, respectively. As weight loss is an important indicator of postharvest freshness associated with fruit transpiration and respiration (Fagundes et al., 2015), this study determined a progressively increased weight loss of cherry tomatoes in all samples during 10-day storage, but the two composite-film packages had consistently lower weight losses than those of the control and PE packages in particular for the last 4-day storages (Fig. 9c). Accordingly, the two composite-film packages maintained higher firmness levels than the control and PE packages (Fig. 9d), indicating a relatively slower fruit softening during storage (D'Aquino et al., 2016). Because the pH value generally increases during cherry tomatoes storage with changes in organic acid metabolism (Tumwesigye et al., 2017), this study detected a gradually increased pH value in all samples during 10-day storage, but two composite film packages maintained lower pH values relative to the control and PE ones (Fig. 9e). Furthermore, a dynamic alteration of TSS (total soluble solids) and Vc (vitamin C) levels was determined in all samples during 10-day storage (Fig. 9f & g), reflecting changes in postharvest quality during storage (Siddiqui et al., 2018). After six days storage, however, two films-packaged tomatoes retained relatively high TSS and Vc levels, whereas the control and PE samples showed a drastic reduction of both TSS and Vc during the later storage period (Locali-Pereira et al., 2021). The relatively higher Vc levels measured in the composite film packages were also consistent with their slower overall quality deterioration. Overall, the packaging system of PVA/5%eCNFs/ε-PL/15%LNPs composite film maintained the most favorable preservation performance among the tested systems, as reflected by the lowest decay rate and better retention of cherry tomato quality during the 10-day storage period.

3.9. Proposed structure-function relationships of PVA/eCNFs/ε-PL/LNPs films

To understand the structure-function relationships underlying the balanced performance of the selected PVA/5%eCNFs/ε-PL/15%LNPs film containing Msa32-derived eCNFs, this study summarized the

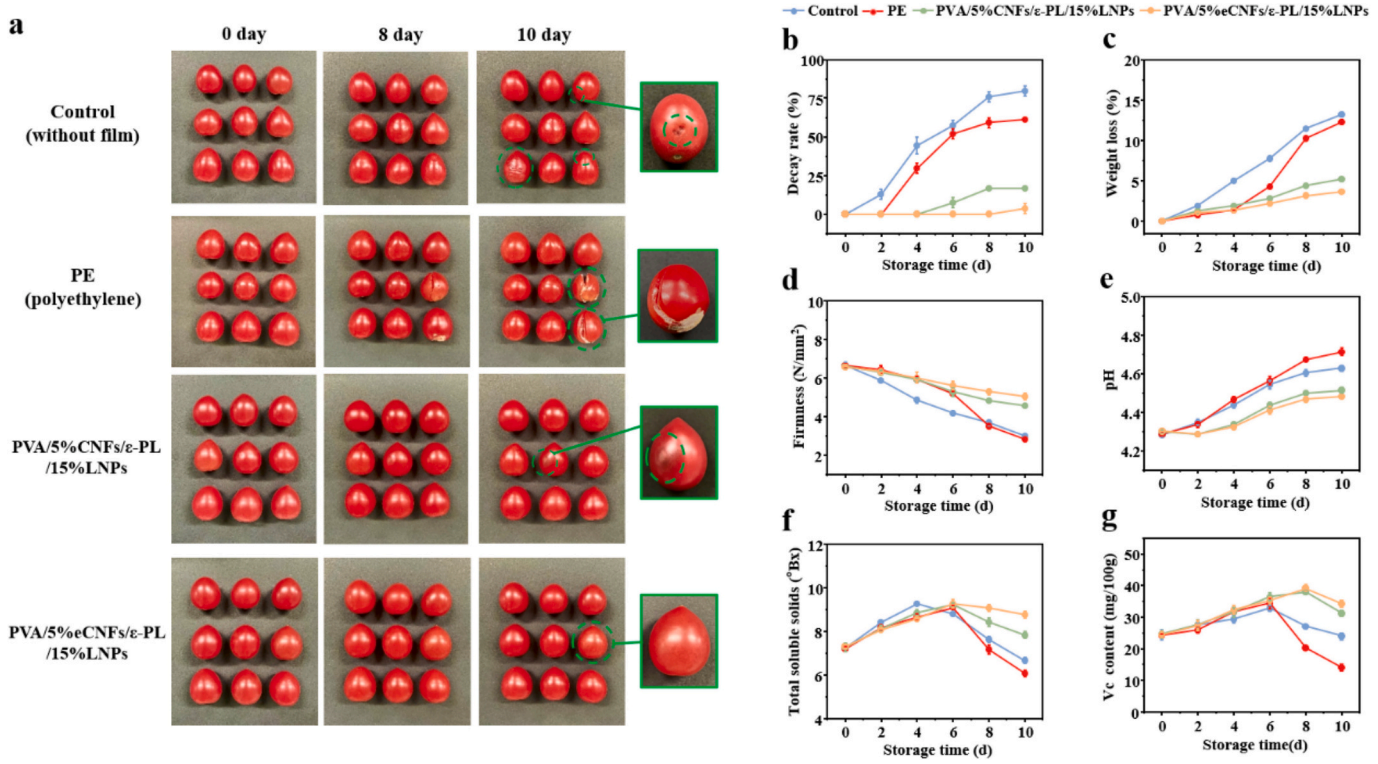


Fig. 9. Preservation performance of the selected composite films for cherry tomatoes during 10 days of storage. (a) Representative appearances of cherry tomatoes under different packaging treatments. (b) Decay rate. (c) Weight loss. (d) Firmness. (e) pH. (f) Total soluble solids (TSS). (g) Vitamin C (Vc) content. Data as mean ± SD ($n = 3$; 18 fruits per container).

experimentally-observed structural features and functional properties (Table 1). In principle, such improved functions and performances of the composite films should be associated with physical interactions among PVA, eCNFs, LNPs and ε-PL, including hydrogen bonding, fibril entanglement, and component packing within the film matrix (Haldar et al., 2026; Moreno & Sipponen, 2024). In particular, synergistic alterations of eCNFs morphology, cellulose DP, residual hemicellulose content, and inter-defect distance (Fig. 2; Table S5-S7) should be accountable for distinct CNFs/LNPs association and film morphology (Fig. 3; Fig. 4). These observations suggested an integrated influence of multiple structural factors on properties of the composite films. Because this study applied short-duration enzymatic tailoring for CNFs assembly before incorporation with LNPs, it could alter fibril morphology, cellulose DP, and polymer composition in the eCNFs (Fig. 1a, b). A conceptual model was further proposed to illustrate possible changes in eCNFs/LNPs interfacial association and physical packing (Fig. 1d), providing an applicable strategy for designing specific composite films. Moreover, the incorporations of PVA, eCNFs, LNPs and ε-PL may form a hydrogen-bonded physical network (Fig. 1e), in which hydrogen bonding, fibril entanglement, and dispersed LNPs domains should contribute to stress transfer and film integrity (Table 1). The relatively compact morphology of the Msa32-derived eCNFs film was consistent with differences in component packing and physical association, which may contribute to its mechanical response. As the elongation at break may be influenced by the mobility of PVA chains and the contribution of ε-PL to film flexibility (Wahid et al., 2019), altered morphology and dispersion of eCNFs should also affect stress distribution, contributing to the high extensibility observed in the selected film (Fig. 1f; Fig. 6). Similarly, the lower WVP and OTR and reduced solubility and swelling examined for the selected formulations were consistent with more tortuous transport pathways and compact physical packing within the multicomponent matrix, which may limit water and gas transport (Fig. 5; Fig. S12) (Zhou et al., 2023).

Given the lignin substrate serves as a key component responsible for UV shielding and antioxidant activity (Yu et al., 2025; Zubair et al., 2024), the aromatic and phenolic structures of LNPs should contribute to UV attenuation and the radical scavenging activity measured after DMSO extraction (He et al., 2023), being consistent with the UVA/UVB blocking and DPPH results (Fig. 8; Table S12). Following exposure to 100 °C and storage at −80 °C, the selected eCNFs-containing film showed a smaller reduction in EAB and relatively stable mechanical properties (Fig. 7), indicating improved mechanical stability after the specified temperature treatments. Consistent with its combined physical and functional properties, the packaging system of selected PVA/5% eCNFs/ε-PL/15%LNPs also resulted in lower decay and weight loss for better maintenance of cherry tomato quality during storage (Fig. 9), thereby revealing a synergistic role of the composite packaging system.

Table 1
Proposed structure-function relationships of the selected PVA/5%eCNFs/ε-PL/15%LNPs film containing Msa32-derived eCNFs.

Functional Property	Key Components	Proposed Contribution
Tensile strength	PVA + eCNFs + LNPs	Hydrogen bonding, fibril entanglement, and LNPs reinforcement
Elongation at break	PVA + eCNFs + ε-PL	PVA chain mobility, ε-PL flexibility, and eCNFs dispersion
Oxygen and water vapor barrier property	eCNFs + LNPs	Tortuous pathways and compact physical packing
Water resistance	eCNFs + LNPs	Hydrogen bonding and compact physical packing
UV-shielding property	LNPs	Aromatic and conjugated structures for UV attenuation
Antioxidant activity	LNPs	Phenolic groups for radical scavenging
Low-temperature mechanical stability (−80 °C)	PVA + eCNFs	Hydrogen-bonded physical network supporting mechanical stability
High-temperature mechanical stability (100 °C)	eCNFs + LNPs	Physical network supporting film integrity
Food preservation performance	All components	Integrated packaging-system effect

4. Conclusion

By selecting the desired *Miscanthus* accession, this study performed controlled enzymatic tailoring of *Miscanthus* lignocellulose for simultaneously altering fibril morphology, cellulose DP, residual hemicellulose content and surface topography of eCNFs. The integration of 5%eCNFs and 15%LNPs was then examined for the desired composite film assembly by co-incorporation with appropriate PVA and ε-PL, which facilitated to fabricate a dense and homogeneous network in the film matrix as supported by AFM, TEM, SEM, FT-IR, and XPS analyses. The selected PVA/5%eCNFs/ε-PL/15%LNPs film exhibited a remarkably improved elongation at break of 255.30% and relatively high tensile strength of 22.54 MPa, together with stable mechanical performance after exposure to extreme high and low temperatures. The film achieved UVA and UVB blocking efficiencies of 87.14% and 98.34%, and also had favorable extractable radical-scavenging activity. In cherry tomato packaging, the selected composite-film system reduced the decay rate to 4% after 10 days of storage. Therefore, this work demonstrated an integrative strategy for the desired composite film construction along with a novel hypothetic model proposed to account for CNFs and LNPs interfacial association, offering an applicable nanotechnology for film design and application.

CRediT authorship contribution statement

Ling Luo: Writing – original draft, Visualization, Software, Methodology, Investigation. **Qian Zhang:** Software, Methodology, Investigation. **Ji Shi:** Software, Methodology, Investigation. **Guilan Zhao:** Software, Methodology, Investigation. **Siqin Tan:** Resources, Investigation. **Jiale Liu:** Resources, Investigation. **Jingyuan Liu:** Resources, Investigation. **Peng Liu:** Writing – review & editing, Investigation. **Hao Peng:** Writing – review & editing, Investigation. **Boyang He:** Writing – review & editing, Investigation. **Jing Wang:** Software, Methodology, Investigation. **Hanluo Li:** Software, Methodology, Investigation. **Yanting Wang:** Writing – review & editing, Methodology, Funding acquisition. **Hua Yu:** Writing – review & editing, Supervision, Funding acquisition. **Liangcai Peng:** Writing – review & editing, Supervision, Funding acquisition, Conceptualization.

Declaration of competing interest

The authors declare that they have no known competing financial interests or personal relationships that could have appeared to influence the work reported in this study.

Acknowledgements

This work was in partial supported by the National Natural Science Foundation of China (32500325 to HY, 32470273 to LP, 32570317 to YW), the Initiative Grant of Hubei University of Technology for High-level Talents (GCC20230001 to LP), and the Hubei Provincial Natural Science Foundation of China for Excellent Young Scientists (2024AFA100 to YW).

Appendix A. Supplementary data

Supplementary data to this article can be found online at https://doi.org/10.1016/j.carbpol.2026.126052.

Data availability

Data will be made available on request.

References

Ai, Y., Wang, H., Liu, P., Yu, H., Sun, M., Zhang, R., Tang, J., Wang, Y., Feng, S., & Peng, L. (2024). Insights into contrastive cellulose nanofibrils assembly and nanocrystals catalysis from dual regulations of plant cell walls. *Science Bulletin, 69*(24), 3815–3819. https://doi.org/10.1016/j.scib.2024.06.013

ASTM. (1996). *Standard test methods for tensile properties of thin plastic sheeting (ASTM D882-91)*. . In Annual Book of ASTM Standards. Philadelphia, PA: American Society for Testing and Materials

Babaeipour, S., Nousiainen, P., Garcia, E. M., Mohammadi, P., Vuoriluoto, M., Kimiaei, E., Koivula, H., & Österberg, M. (2025). Oxidative crosslinking for the development of barrier coatings utilizing lignin-containing cellulose nanofibrils and lignin nanoparticles. *Food Packaging and Shelf Life, 49*, Article 101538. https://doi.org/10.1016/j.fpsl.2025.101538

Baishya, H., Dutta, J., & Kumar, S. (2025). Nanofillers reinforcing biopolymer composites for sustainable food packaging applications: A state-of-the-art review. *Advanced Functional Materials, 35*(47), Article 2503819. https://doi.org/10.1002/adfm.202503819

Bhargava, N., Sharanagat, V. S., Mor, R. S., & Kumar, K. (2020). Active and intelligent biodegradable packaging films using food and food waste-derived bioactive compounds: A review. *Trends in Food Science & Technology, 105*, 385–401. https://doi.org/10.1016/j.tifs.2020.09.015

Chen, K., Xu, G., Tian, R., Jiang, J., Wu, K., Kuang, Y., & Jiang, F. (2023). Development of konjac glucomannan based *Syringa* essential oil film and its fragmented form for quality maintenance of citrus fruits. *Food Packaging and Shelf Life, 40*, Article 101185. https://doi.org/10.1016/j.fpsl.2023.101185

D'Aquino, S., Mistriotis, A., Briassoulis, D., Di Lorenzo, M. L., Malinconico, M., & Palma, A. (2016). Influence of modified atmosphere packaging on postharvest quality of cherry tomatoes held at 20°C. *Postharvest Biology and Technology, 115*, 103–112. https://doi.org/10.1016/j.postharvbio.2015.12.014

Deng, N., Ma, Y., Li, P., Zeng, J., Gong, Z., Su, J., Li, J., Cao, D., Wang, B., Xu, J., & Chen, K. (2025). Mechanically robust lignin-cellulose films with triple barrier functions for antagonistic food preservation. *Chemical Engineering Journal, 521*, Article 166561. https://doi.org/10.1016/j.cej.2025.166561

Fagundes, C., Moraes, K., Pérez-Gago, M. B., Palou, L., Maraschin, M., & Monteiro, A. R. (2015). Effect of active modified atmosphere and cold storage on the postharvest quality of cherry tomatoes. *Postharvest Biology and Technology, 109*, 73–81. https://doi.org/10.1016/j.postharvbio.2015.05.017

Fan, Y., Ren, J., Cao, Y., Zou, Y., Xiao, X., & Liu, F. (2025). Recent advances in polyvinyl alcohol-based biodegradable packaging: Preparation, modification, and applications in food packaging. *Comprehensive Reviews in Food Science and Food Safety, 24*(6), Article e70334. https://doi.org/10.1111/1541-4337.70334

Gao, B., Yu, J., Luo, L., Zhu, L., Tang, Z., Wang, Y., Kang, J., Sun, D., Peng, H., Wang, Y., Peng, L., & Yu, H. (2026). Cascading valorization of *Miscanthus* biomass for bioethanol, lactic acid and nanomaterials via green-like pretreatment with reusable fertilizers. *Renewable Energy, 264*, Article 125555. https://doi.org/10.1016/j.renene.2026.125555

Guzman-Puyol, S., Hierrezuelo, J., Benítez, J. J., Tedeschi, G., Porras-Vázquez, J. M., Heredia, A., Athanassiou, A., Romero, D., & Heredia-Guerrero, J. A. (2022). Transparent, UV-blocking, and high barrier cellulose-based bioplastics with naringin as active food packaging materials. *International Journal of Biological Macromolecules, 209*, 1985–1994. https://doi.org/10.1016/j.ijbiomac.2022.04.177

Haghighi, H., Gullo, M., La China, S., Pfeifer, F., Siesler, H. W., Licciardello, F., & Pulvirenti, A. (2021). Characterization of bio-nanocomposite films based on gelatin/polyvinyl alcohol blend reinforced with bacterial cellulose nanowhiskers for food packaging applications. *Food Hydrocolloids, 113*, Article 106454. https://doi.org/10.1016/j.foodhyd.2020.106454

Haldar, S., Kusuma, V. K., Banerjee, S., & Misal, P. R. (2026). Formulation of tamarind polysaccharide-lignin-PVA based biodegradable films using response surface methodology (RSM). *International Journal of Biological Macromolecules, 343*, Article 150430. https://doi.org/10.1016/j.ijbiomac.2026.150430

Han, X., Wang, Q., Mi, J., Zhang, J., Feng, J., Du, T., Luo, L., Zhang, C., Wang, J., & Zhang, W. (2025). ε-Polylysine-mediated assembly regulating the band gap of natural polyphenols for boosted photodynamic antimicrobial effect. *Chemical Engineering Journal, 507*, Article 160420. https://doi.org/10.1016/j.cej.2025.160420

He, Y., Ye, H.-C., You, T.-T., & Xu, F. (2023). Sustainable and multifunctional cellulose-lignin films with excellent antibacterial and UV-shielding for active food packaging. *Food Hydrocolloids, 137*, Article 108355. https://doi.org/10.1016/j.foodhyd.2022.108355

Hou, Y., Guan, Q.-F., Xia, J., Ling, Z.-C., He, Z., Han, Z.-M., Yang, H.-B., Gu, P., Zhu, Y., Yu, S.-H., & Wu, H. (2021). Strengthening and toughening hierarchical nanocellulose via humidity-mediated interface. *ACS Nano, 15*(1), 1310–1320. https://doi.org/10.1021/acsnano.0c08574

Jailani, A., Hidzer, M. H., Firdaus, A. H. M., Sapuan, S. M., Zainudin, E. S., Atiqah, A., Wan Jaafar, W. M., & Suryanegara, L. (2026). Enhancing polyvinyl alcohol (PVA) nanocomposites: Key properties, applications and challenges in advanced engineering. *Defence Technology, 55*, 11–29. https://doi.org/10.1016/j.dt.2025.05.020

Kalita, P., Bora, N. S., Gogoi, B., Goswami, A., Pachuau, L., Das, P. J., Baishya, D., & Roy, S. (2025). Improving the hydrophobic nature of biopolymer based edible packaging film: A review. *Food Chemistry, 479*, Article 143793. https://doi.org/10.1016/j.foodchem.2025.143793

Las-Casas, B., Wu, J., Rojas, O. J., & Arantes, V. (2025). Exploring lignin nanoparticle incorporation to develop multifunctional cellulose nanofibril films for active packaging. *International Journal of Biological Macromolecules, 323*, Article 147013. https://doi.org/10.1016/j.ijbiomac.2025.147013

Lee, H., You, J., Jin, H.-J., & Kwak, H. W. (2020). Chemical and physical reinforcement behavior of dialdehyde nanocellulose in PVA composite film: A comparison of nanofiber and nanocrystal. *Carbohydrate Polymers, 232*, Article 115771. https://doi.org/10.1016/j.carbpol.2019.115771

Li, H., Kulachenko, A., Mathew, A. P., Stoltz, R. B., & Sevastyanova, O. (2023). Enhancing the strength and flexibility of microfibrillated cellulose films from lignin-rich kraft pulp. *ACS Sustainable Chemistry & Engineering, 11*(47), 16793–16805. https://doi.org/10.1021/acssuschemeng.3c05086

Li, J., Wang, Y., Zhou, Y., Tan, S., Liu, J., Zhang, Q., Yang, R., Peng, H., Liu, P., Wang, Y., Peng, L., & Kang, H. (2026). Integrative mechanisms of Mn peroxidase-dominated fungal digestion and CaO depolymerization for synergistic enhancement of biomass saccharification towards distinct bioethanol and lactic acid conversions in desired *Miscanthus*. *Industrial Crops and Products, 246*, Article 123224. https://doi.org/10.1016/j.indcrop.2026.123224

Li, Q., Xie, B., Wang, Y., Wang, Y., Peng, L., Li, Y., Li, B., & Liu, S. (2019). Cellulose nanofibrils from *Miscanthus floridulus* straw as green particle emulsifier for O/W Pickering emulsion. *Food Hydrocolloids, 97*, Article 105214. https://doi.org/10.1016/j.foodhyd.2019.105214

Locali-Pereira, A. R., Guazi, J. S., Conti-Silva, A. C., & Nicoletti, V. R. (2021). Active packaging for postharvest storage of cherry tomatoes: Different strategies for application of microencapsulated essential oil. *Food Packaging and Shelf Life, 29*, Article 100723. https://doi.org/10.1016/j.fpsl.2021.100723

Lu, S., Sun, L., Wang, Y., Peng, H., He, B., Yuan, X., Wang, Y., Xia, T., Peng, L., & Liu, P. (2026). Dual-upgraded biomass saccharification and bioethanol production by cascading peptides interactions with polymers and activating cellulases in bioenergy crops. *Renewable Energy, 256*, Article 124651. https://doi.org/10.1016/j.renene.2025.124651

Mai, X., Zhang, X., Wang, W., Zheng, Y., Wang, D., Xu, W., Liu, F., & Sun, Z. (2023). Novel PVA/carboxylated cellulose antimicrobial hydrogel grafted with curcumin and ε-polylysine for chilled chicken preservation. *Food Chemistry, 424*, Article 136345. https://doi.org/10.1016/j.foodchem.2023.136345

Moreno, A., & Sipponen, M. H. (2024). Overcoming challenges of lignin nanoparticles: Expanding opportunities for scalable and multifunctional nanomaterials. *Accounts of Chemical Research, 57*(14), 1918–1930. https://doi.org/10.1021/acs.accounts.4c00206

Narasagoudr, S. S., Hegde, V. G., Vanjeri, V. N., Chougale, R. B., & Masti, S. P. (2020). Ethyl vanillin incorporated chitosan/poly(vinyl alcohol) active films for food packaging applications. *Carbohydrate Polymers, 236*, Article 116049. https://doi.org/10.1016/j.carbpol.2020.116049

Ning, Y., Yang, W., Liu, S., Xu, J., Cheng, X., Xu, S., Li, J., & Wang, L. (2025). A fluorescent polyvinyl alcohol film with efficient photodynamic antimicrobial performance enabled by berberine/phytic acid salt for food preservation. *Advanced Functional Materials, 35*(1), Article 2411314. https://doi.org/10.1002/adfm.202411314

Österberg, M., Henn, K. A., Farooq, M., & Valle-Delgado, J. J. (2023). Biobased nanomaterials—the role of interfacial interactions for advanced materials. *Chemical Reviews, 123*(5), 2200–2241. https://doi.org/10.1021/acs.chemrev.2c00492

Oun, A. A., Shin, G. H., Rhim, J.-W., & Kim, J. T. (2022). Recent advances in polyvinyl alcohol-based composite films and their applications in food packaging. *Food Packaging and Shelf Life, 34*, Article 100991. https://doi.org/10.1016/j.fpsl.2022.100991

Pei, J., Wang, Y., Zhang, Q., Yu, J., Sun, P., & Wang, Y. (2025). A novel water-soluble antibacterial films of gelatin/carboxymethyl cellulose sodium incorporated with *Grifola frondosa* polysaccharides and pearl powder for fruit preservation. *International Journal of Biological Macromolecules, 311*, Article 143704. https://doi.org/10.1016/j.ijbiomac.2025.143704

Peng, H., Zhao, W., Liu, J., Liu, P., Yu, H., Deng, J., Yang, Q., Zhang, R., Hu, Z., Liu, S., Sun, D., Peng, L., & Wang, Y. (2022). Distinct cellulose nanofibrils generated for improved Pickering emulsions and lignocellulose-degradation enzyme secretion coupled with high bioethanol production in natural rice mutants. *Green Chemistry, 24*(7), 2975–2987. https://doi.org/10.1039/D1GC04447H

Peng, J., Fu, R., Huang, Y., Lu, J., Xie, X., Xue, Z., Chen, M., Wu, X., Yue, H., & Mai, H. (2025). Influence and mechanism of NaOH concentration on the dissolution of cellulose and extraction of CNF in alkaline solvents at 15°C. *Carbohydrate Polymers, 353*, Article 123265. https://doi.org/10.1016/j.carbpol.2025.123265

Priyadarshi, R., Ghosh, T., Purohit, S. D., Prasannavenkadesan, V., & Rhim, J.-W. (2024). Lignin as a sustainable and functional material for active food packaging applications: A review. *Journal of Cleaner Production, 469*, Article 143151. https://doi.org/10.1016/j.jclepro.2024.143151

Siddiqui, M. W., Lara, I., Ilahy, R., Tlili, I., Ali, A., Homa, F., Prasad, K., Deshi, V., Lenucci, M. S., & Hdider, C. (2018). Dynamic changes in health-promoting properties and eating quality during off-vine ripening of tomatoes. *Comprehensive Reviews in Food Science and Food Safety, 17*(6), 1540–1560. https://doi.org/10.1111/1541-4337.12395

Sun, Y., Li, M., Yang, M., Xia, W., Wang, S., Wang, Z., Wang, Y., Peng, L., Hu, H., & Zhang, R. (2026). Engineered cytosolic and chloroplastic UDP-glucose epimerases distinctly modulate xylan interplay for size-tunable cellulose nanocrystals

production in Oryza sativa. *Carbohydrate Polymers, 375*, Article 124803. https://doi.org/10.1016/j.carbpol.2025.124803

Tang, Y., Zhang, X., Zhao, R., Guo, D., & Zhang, J. (2018). Preparation and properties of chitosan/guar gum/nanocrystalline cellulose nanocomposite films. *Carbohydrate Polymers, 197*, 128–136. https://doi.org/10.1016/j.carbpol.2018.05.073

Trifol, J., & Moriana, R. (2022). Barrier packaging solutions from residual biomass: Synergetic properties of CNF and LCNF in films. *Industrial Crops and Products, 177*, Article 114493. https://doi.org/10.1016/j.indcrop.2021.114493

Trigui, K., Magnin, A., Putaux, J.-L., & Boufi, S. (2025). Poly(vinyl alcohol)/oxidized cellulose nanofibril composite films with high nanofiller content for enhanced packaging applications. *Journal of Industrial and Engineering Chemistry, 148*, 602–613. https://doi.org/10.1016/j.jiec.2025.01.016

Tumwesigye, K. S., Sousa, A. R., Oliveira, J. C., & Sousa-Gallagher, M. J. (2017). Evaluation of novel bitter cassava film for equilibrium modified atmosphere packaging of cherry tomatoes. *Food Packaging and Shelf Life, 13*, 1–14. https://doi.org/10.1016/j.fpsl.2017.04.007

Turan, D., Keukens, B. M., & Schifferstein, H. N. J. (2024). Food packaging technology considerations for designers: Attending to food, consumer, manufacturer, and environmental issues. *Comprehensive Reviews in Food Science and Food Safety, 23*(6), Article e70058. https://doi.org/10.1111/1541-4337.70058

United States Pharmacopeial Convention. (2002). *The United States Pharmacopeia 25-National Formulary 20 (USP 25-NF 20)*. Rockville, MD: United States Pharmacopeial Convention, Inc.

Upadhyay, A., Agbesi, P., Arafat, K. M. Y., Urdaneta, F., Dey, M., Basak, M., Hong, S., Umeileka, C., & Argyropoulos, D. (2024). Bio-based smart packaging: Fundamentals and functions in sustainable food systems. *Trends in Food Science & Technology, 145*, Article 104369. https://doi.org/10.1016/j.tifs.2024.104369

Wahid, F., Wang, F.-P., Xie, Y.-Y., Chu, L.-Q., Jia, S.-R., Duan, Y.-X., Zhang, L., & Zhong, C. (2019). Reusable ternary PVA films containing bacterial cellulose fibers and ε-polylysine with improved mechanical and antibacterial properties. *Colloids and Surfaces B: Biointerfaces, 183*, Article 110486. https://doi.org/10.1016/j.colsurfb.2019.110486

Wan, Z., Zhang, H., Niu, M., Zhang, W., Guo, Y., & Li, H. (2025). Preparation of lignin nanoparticles by ultrasonication and its incorporation in DLP 3D printing UV-curable resin as bio-filler. *Industrial Crops and Products, 224*, Article 120394. https://doi.org/10.1016/j.indcrop.2024.120394

Wang, M., Wang, Y., Liu, J., Yu, H., Liu, P., Yang, Y., Sun, D., Kang, H., Wang, Y., Tang, J., Fu, C., & Peng, L. (2024). Integration of advanced biotechnology for green carbon. *Green Carbon, 2*(2), 164–175. https://doi.org/10.1016/j.greenca.2024.02.006

Wang, Y., Fan, C., Hu, H., Li, Y., Sun, D., Wang, Y., & Peng, L. (2016). Genetic modification of plant cell walls to enhance biomass yield and biofuel production in bioenergy crops. *Biotechnology Advances, 34*(5), 997–1017. https://doi.org/10.1016/j.biotechadv.2016.06.001

Wang, Z., Qiao, X., & Sun, K. (2018). Rice straw cellulose nanofibrils reinforced poly (vinyl alcohol) composite films. *Carbohydrate Polymers, 197*, 442–450. https://doi.org/10.1016/j.carbpol.2018.06.025

Wei, D., Liang, S., Lv, S., Zuo, J., Liu, L., & Zhang, S. (2024). Dodecyl sulphide silane-modified SiO_2/lignin-based carbon nanoparticles superhydrophobic and UV-resistant composite coatings. *Journal of Environmental Chemical Engineering, 12*(5), Article 113647. https://doi.org/10.1016/j.jece.2024.113647

Worku, L. A., Tadesse, M. G., Bachheti, A., Pandey, D. P., Chandel, A. K., Ewuntu, A. W., & Bachheti, R. K. (2024). Experimental investigations on PVA/chitosan and PVA/chitin films for active food packaging using *Oxytenanthera abyssinica* lignin nanoparticles and its UV-shielding, antimicrobial, and antiradical effects. *International Journal of Biological Macromolecules, 254*, Article 127644. https://doi.org/10.1016/j.ijbiomac.2023.127644

Wu, K., Yan, X., Zhu, D., Tao, Y., Zeng, Y., Li, X., Sun, W., Qian, H., Jiang, F., & Chen, S. (2023). Formation and characterization of konjac glucomannan/ethyl cellulose films by using ethanol and water as the solvents. *International Journal of Biological Macromolecules, 241*, Article 124629. https://doi.org/10.1016/j.ijbiomac.2023.124629

Xiang, F., Xia, Y., Wang, Y., Wang, Y., Wu, K., & Ni, X. (2021). Preparation of konjac glucomannan based films reinforced with nanoparticles and its effect on cherry tomatoes preservation. *Food Packaging and Shelf Life, 29*, Article 100701. https://doi.org/10.1016/j.fpsl.2021.100701

Xiao, M., Luo, L., Tang, B., Qin, J., Wu, K., & Jiang, F. (2022). Physical, structural, and water barrier properties of emulsified blend film based on konjac glucomannan/agar/gum Arabic incorporating virgin coconut oil. *LWT, 154*, Article 112683. https://doi.org/10.1016/j.lwt.2021.112683

Yang, J., Punia Bangar, S., Rizwan Khan, M., Hammouda, G. A., Alam, P., & Zhang, W. (2024). Biopolymer-based packaging films/edible coatings functionalized with ε-polylysine: New options for food preservation. *Food Research International, 187*, Article 114390. https://doi.org/10.1016/j.foodres.2024.114390

Yang, R., Su, Y., Li, J., Zhou, Y., Wang, Y., Tan, S., Liu, J., Wang, Y., Sun, D., Xia, T., Kang, H., & Peng, L. (2026). Biomass saccharification of bioenergy crops enhanced by selective soybean proteins for distinct cellulosic ethanol and lactic acid conversions with high Cd^{2+} adsorption. *Industrial Crops and Products, 240*, Article 122534. https://doi.org/10.1016/j.indcrop.2025.122534

Yu, H., Hu, M., Hu, Z., Liu, F., Yu, H., Yang, Q., Gao, H., Xu, C., Wang, M., Zhang, G., Wang, Y., Xia, T., Peng, L., & Wang, Y. (2022). Insights into pectin dominated enhancements for elimination of toxic Cd and dye coupled with ethanol production in desirable lignocelluloses. *Carbohydrate Polymers, 286*, Article 119298. https://doi.org/10.1016/j.carbpol.2022.119298

Yu, H., Lanot, A., & Mao, N. (2024). The relationship between molecular weight of bacterial cellulose and the viscosity of its copper (II) ethylenediamine solutions. *Cellulose, 31*, 7973–7992. https://doi.org/10.1007/s10570-024-06106-1

Yu, H., Zhang, G., Liu, J., Liu, P., Peng, H., Teng, Z., Li, Y., Ren, X., Fu, C., Tang, J., Li, M., Wang, Y., Wang, L., & Peng, L. (2025). A functional cascading of lignin modification via repression of caffeic acid *O*-methyltransferase for bioproduction and anti-oxidation in rice. *Journal of Advanced Research, 78*, 1–9. https://doi.org/10.1016/j.jare.2025.01.048

Yu, J., Tang, Z., Zhu, L., Gao, B., Hong, J., Fang, Y., Kang, J., Sun, D., Peng, H., He, B., Bakr, M. M. A., Wang, Y., Peng, L., & Yu, H. (2026). Low-temperature $ZnCl_2$ activation of distinct *Miscanthus* lignin as highly-porous biochar assembly for efficient removal of organic dyes, tetracycline and Cr(VI). *Industrial Crops and Products, 240*, Article 122630. https://doi.org/10.1016/j.indcrop.2026.122630

Yu, M., Hou, Y., Zheng, L., Han, Y., & Wang, D. (2023). Soy protein isolate-based active films functionalized with *Zanthoxylum bungeanum* by-products: Effects on barrier, mechanical, antioxidant and cherry tomato preservation performance. *International Journal of Biological Macromolecules, 253*, Article 127539. https://doi.org/10.1016/j.ijbiomac.2023.127539

Zhai, W., Zhong, Y., Xu, M., Wei, X., Cai, L., Xia, C., & Wei, Y. (2024). An antioxidant, reusable laser printed and recycled cork paper packaging. *Advanced Functional Materials, 34*(34), Article 2401820. https://doi.org/10.1002/adfm.202401820

Zhang, P., Zhao, Y., & Shi, Q. (2016). Characterization of a novel edible film based on gum ghatti: Effect of plasticizer type and concentration. *Carbohydrate Polymers, 153*, 345–355. https://doi.org/10.1016/j.carbpol.2016.07.082

Zhang, R., Gao, H., Wang, Y., He, B., Lu, J., Zhu, W., Peng, L., & Wang, Y. (2023). Challenges and perspectives of green-like lignocellulose pretreatments selectable for low-cost biofuels and high-value bioproduction. *Bioresource Technology, 369*, Article 128315. https://doi.org/10.1016/j.biortech.2022.128315

Zhang, R., Hu, Z., Peng, H., Liu, P., Wang, Y., Li, J., Lu, J., Wang, Y., Xia, T., & Peng, L. (2023). High density cellulose nanofibril assembly leads to upgraded enzymatic and chemical catalysis of fermentable sugars, cellulose nanocrystals and cellulase production by precisely engineering cellulose synthase complexes. *Green Chemistry, 25*(3), 1096–1106. https://doi.org/10.1039/D2GC03744K

Zhang, R., Hu, Z., Wang, Y., Hu, H., Li, F., Li, M., Ragauskas, A., Xia, T., Han, H., Tang, J., Yu, H., Xu, B., & Peng, L. (2023). Single-molecular insights into the breakpoint of cellulose nanofibers assembly during saccharification. *Nature Communications, 14*(1), Article 1100. https://doi.org/10.1038/s41467-023-36856-8

Zhao, G., Zhang, Q., Wang, Y., Gao, X., Huang, F., Liu, J., Peng, H., Fu, C., Wang, Y., & Peng, L. (2026). Optimal integration of lignin nanoparticles and whey protein distinctively stabilizes high internal phase pickering emulsions for multiple environmental resistances. *Food Chemistry, 508*, Article 148452. https://doi.org/10.1016/j.foodchem.2026.148452

Zheng, Q., Bai, X., Chen, T., Li, F., Zhu, P., Li, M., & Tang, Y. (2024). Carboxymethyl hemicellulose/sorbitol/gallic acid green composite films for fresh fruit preservation. *Industrial Crops and Products, 218*, Article 119013. https://doi.org/10.1016/j.indcrop.2024.119013

Zhou, Y., Han, Y., Xu, J., Han, W., Gu, F., Sun, K., Huang, X., & Cai, Z. (2023). Strong, flexible and UV-shielding composite polyvinyl alcohol films with wood cellulose skeleton and lignin nanoparticles. *International Journal of Biological Macromolecules, 232*, Article 123105. https://doi.org/10.1016/j.ijbiomac.2022.12.324

Zubair, M., Rauf, Z., Fatima, S., & Ullah, A. (2024). Lignin-derived bionanocomposites as functional food packaging materials. *Sustainable Food Technology, 2*(4), 945–966. https://doi.org/10.1039/D4FB00105B